

Chemical Variation in Molecular Cloud Cores in the Orion A Cloud. II.

Ken'ichi TATEMATSU,^{1,2} Satoshi OHASHI,³ Tomofumi UMEMOTO,^{1,2} Jeong-Eun LEE,⁴ Tomoya HIROTA,^{1,2} Satoshi YAMAMOTO,⁵ Minhoo CHOI,⁶ Ryo KANDORI,¹ and Norikazu MIZUNO^{1,3}

¹*National Astronomical Observatory of Japan, 2-21-1 Osawa, Mitaka, Tokyo 181-8588*

²*Department of Astronomical Science, The Graduate University for Advanced Studies (Sokendai), 2-21-1 Osawa, Mitaka, Tokyo 181-8588*

³*Department of Astronomy, The University of Tokyo, Bunkyo-ku, Tokyo 113-0033*

⁴*School of Space Research, Kyung Hee University, Seocheon-Dong, Giheung-Gu, Yongin-Si, Gyeonggi-Do, 446-701, South Korea*

⁵*Department of Physics, The University of Tokyo, Bunkyo-ku, Tokyo 113-0033*

⁶*Korea Astronomy and Space Science Institute, Daedeokdaero 776, Yuseong, Daejeon 305-348, South Korea*

k.tatematsu@nao.ac.jp, satoshi.ohashi@nao.ac.jp, umemoto.tomofumi@nao.ac.jp, jeongeun.lee@khu.ac.kr, tomoya.hirota@nao.ac.jp, yamamoto@taurus.phys.s.u-tokyo.ac.jp, minho@kasi.re.kr, r.kandori@nao.ac.jp, norikazu.mizuno@nao.ac.jp

(Received 2013 June 17; accepted 2013 September 19)

Abstract

We have mapped six molecular cloud cores in the Orion A giant molecular cloud (GMC), whose kinetic temperatures range from 10 to 30 K, in CCS and N₂H⁺ with Nobeyama 45 m radio telescope to study their chemical characteristics. We identified 31 intensity peaks in the CCS and N₂H⁺ emission in these molecular cloud cores. It is found for cores with temperatures lower than ~ 25 K that the column density ratio of $N(\text{N}_2\text{H}^+)/N(\text{CCS})$ is low toward starless core regions while it is high toward star-forming core regions, in case that we detected both of the CCS and N₂H⁺ emission. This is very similar to the tendency found in dark clouds (kinetic temperature ~ 10 K). The criterion found in the Orion A GMC is $N(\text{N}_2\text{H}^+)/N(\text{CCS}) \sim 2 - 3$. In some cases, the CCS emission is detected toward protostars as well as the N₂H⁺ emission. Secondary late-stage CCS peak in the chemical evolution caused by CO depletion may be a possible explanation for this. We found that the chemical variation of CCS and N₂H⁺ can also be used as a tracer of evolution in warm (10–25 K) GMC cores. On the other hand, some protostars do not accompany N₂H⁺ intensity peaks but are associated with dust continuum emitting regions, suggesting that the N₂H⁺ abundance might be decreased due to CO evaporation in warmer star-forming sites.

Key words: ISM: clouds —ISM: individual (Orion Nebula, Orion Molecular Cloud) —ISM: molecules —ISM: structure—stars: formation

1. Introduction

In nearby dark clouds, molecules such as CCS, HC₃N, NH₃, and N₂H⁺, and the neutral carbon atom C⁰ are known to be good tracers of the chemical evolution (e.g., Hirahara et al. 1992; Suzuki et al. 1992; Benson, Caselli, & Myers 1998; Maezawa et al. 1999; Lai & Crutcher 2000; Hirota, Ito, & Yamamoto 2002; Hirota, Ohishi, & Yamamoto 2009). The carbon-chain molecules, CCS and HC₃N trace the early chemical evolutionary stage, whereas N-bearing molecules, NH₃ and N₂H⁺ trace the late stage. On the other hand, the chemical evolution of molecular cloud cores in giant molecular clouds (GMCs) is less understood, compared with that of nearby dark cloud cores. Most of stars in the Galaxy form in GMCs, and then the chemical evolution of molecular cloud cores in them is of our great interest to study the star forming process in the Galaxy. We wonder how different the chemical properties of molecular cloud cores in GMCs are, compared with those in nearby dark clouds. Dark clouds and GMCs are different in their physical properties and associated star formation (e.g., Turner 1988). GMCs are larger, more massive and warmer than dark clouds. Dark clouds show only isolated low-mass star formation, but GMCs show massive star formation and formation of star clusters.

The Orion A cloud is an archetypal GMC. Ungerechts et al. (1997) studied the region near Orion KL in many molecular lines, and have shown difference in the molecular abundances among the Orion KL region, the Orion Bar, and the molecular ridge. Tatematsu et al. (1993a) mapped the Orion A giant molecular cloud in CS $J = 1-0$ and have shown the chemical variation between Orion KL and OMC-2 by comparing the distribution of CS with that of NH₃. Tatematsu et al. (2008) showed that the N₂H⁺ emission is widely distributed over the f -shaped filament of the Orion A GMC, and pointed out that there is 2 arcmin (0.3 pc)-scale displacement between the HC₃N and N₂H⁺ distribution near X-ray emitting protostars in the OMC-3 region at the northern end of the Orion A GMC. Tatematsu et al. (2010) made single-point observations toward the cloud core centers in the Orion A cloud cataloged by Tatematsu et al. (1993a), and detected the CCS emission in $\sim 30\%$ of them. They discussed the chemical variation in this cloud on the basis of the column density ratio of NH₃ to CCS and that of DNC to HN¹³C. They found that the NH₃/CCS and DNC/HN¹³C column density ratios are lower toward regions with warmer temperatures and that the NH₃/CCS column density ratio shows a global variation along the Orion A GMC filament. Johnstone, Boonman, & van Dishoeck (2003) compared submillimeter dust continuum sources in the Orion A GMC with the line emission from other molecules such as CO, H₂CO, and CH₃OH.

In this study, we investigate the chemical characteristics of molecular cloud cores in the Orion A GMC through new mapping observations of CCS and N₂H⁺. The purpose of this

study is to investigate whether our knowledge of the chemical evolution found in cold dark clouds (with kinetic temperatures $T_k \sim 10$ K; see, e.g., Benson, Caselli, & Myers 1998, Hirota, Ohishi, & Yamamoto 2009 and references therein) is valid also for cores in Orion A GMC ($T_k \sim 10\text{--}30$ K) or not.

The distance to the Orion A cloud is estimated to be 418 pc (Kim et al. 2008). At this distance, 1 arcmin corresponds to 0.12 pc.

2. Observations

Observations were carried out by using the 45 m radio telescope of Nobeyama Radio Observatory¹ from 2013 January 13 to 24. The employed receiver front end was the single-beam two-polarization two-sideband-separation (2SB) SIS receiver “TZ1”. We observed CCS $J_N = 7_6 - 6_5$ at 81.505208 GHz (Hirota & Yamamoto 2006) in both of the linear polarizations and N_2H^+ $J = 1-0$ at 93.1737767GHz (Caselli, Myers, & Thaddeus 1995) in the V (vertical) polarization, simultaneously. The upper energy level E_u for these transitions are 15.3 and 4.3 K, respectively. The FWHM beam size and main-beam efficiency η_{MB} of the telescope were 19.1 ± 0.3 arcsec and $41 \pm 3\%$ at 86 GHz, respectively. The receiver back end was the digital spectrometer “SAM45”. The spectral resolution was 30.52 kHz (corresponding to ~ 0.1 km s^{-1}). Spectra were obtained at spacings of 20 arcsec and in the position-switching mode. The employed off position was $(\Delta R. A., \Delta Dec.) = (-30', 0')$ with respect to the map center taken from the core catalog of Tatematsu et al. (1993a). The observed intensity is reported in terms of the corrected antenna temperature T_A^* . To derive the physical parameters, we use the main-beam radiation temperature $T_R = T_A^*/\eta_{MB}$. The telescope pointing was established by observing Orion KL in the 43-GHz SiO maser line every 60–80 min.

We selected 14 cores toward which CCS $J_N = 4_3 - 3_2$ at 45.379033 GHz was detected in the single pointing observation of Tatematsu et al. (2010). The upper energy level E_u for CCS $J_N = 4_3 - 3_2$ is 5.4 K. The selected cores are TUKH003, 021, 040, 049, 056, 059, 069, 083, 088, 097, 104, 105, 117, and 122. Table 1 lists the map centers and employed off positions. First, we have made observations toward 3×3 positions at spacings of 20 arcsec centered at each of the 14 cores. Out of the 14 observed cores, we have detected the 82 GHz CCS emission in 7 cores (TUKH003, 021, 088, 097, 105, 117, and 122). Out of these 7 cores, we have mapped larger area for 6 cores also at spacings of 20 arcsec. A larger map was not carried out for the remaining core TUKH105 due to limited observing time. The average rms noise level in the 82 GHz CCS observations toward 14 cores are 0.057 ± 0.012 K at 30.52 kHz resolution (the rms noise level for maps of each core will be shown later). That in the N_2H^+ observations is about $\sqrt{2}$ higher because the observations were made in a single polarization. Figure 1 shows the location of the six mapped cores illustrated on the CS $J = 1-0$ map (Tatematsu et al. 1993a and additional data, <http://alma.mtk.nao.ac.jp/~kt/fits.html>).

The observed data were reduced by using the software package “NewStar” of Nobeyama Radio Observatory.

¹ Nobeyama Radio Observatory is a branch of the National Astronomical Observatory of Japan, National Institutes of Natural Sciences.

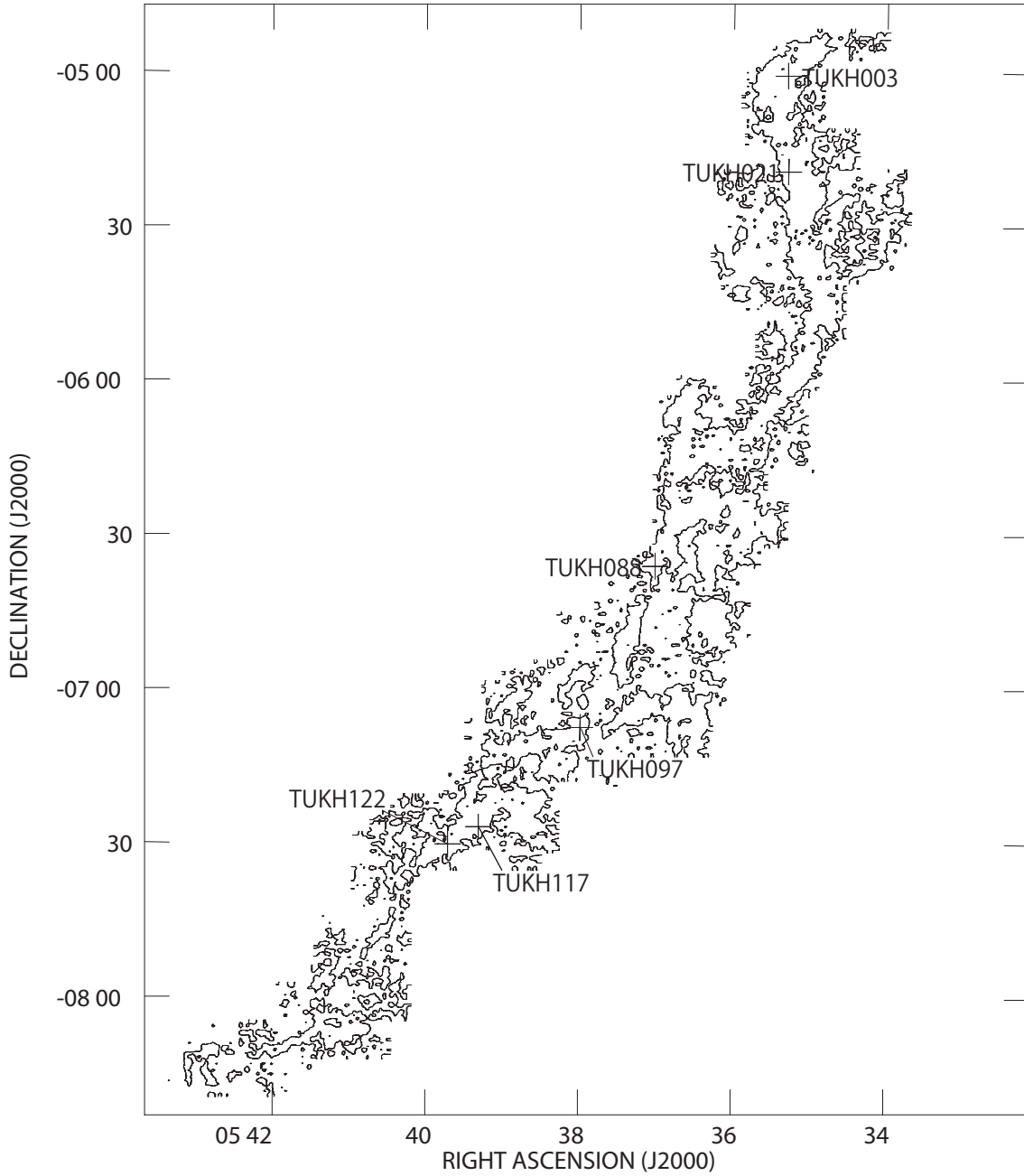


Fig. 1. The locations of the six cores mapped in the present study. The contour is 1.02 K (3σ) of the CS $J = 1-0$ peak intensity map (Tatematsu et al. 1993a and additional data, <http://alma.mtk.nao.ac.jp/~kt/fits.html>).

3. Results and Discussion

3.1. Line Intensities and Their Variations

Figures 2 to 7 show the CCS $J_N = 7_6 - 6_5$ contour maps superimposed on the N_2H^+ $J = 1-0$ gray-scale maps. We plot protostars and their candidates taken from the Spitzer YSO (young stellar object) catalog of the Orion A and B GMCs based on IRAC and MIPS observations (Megeath et al. 2012). These authors carried out the protostar identification based on the colors constructed from IRAC and MIPS data and classified them into protostars (P), faint candidate protostars (FP), and red candidate protostars (RP, objects that show MIPS detections at $24 \mu\text{m}$ but no detections at the 4.5 , 5.8 or $8 \mu\text{m}$ IRAC bands). These sources are thought to be Class 0, I, or flat spectrum (with the spectral index determined between the 4.5 , 5.8 , and $8 \mu\text{m}$ IRAC bands and the $24 \mu\text{m}$ MIPS band; Megeath et al. 2012 and references therein).

In the core regions shown in Figures 2–7, there is no red candidate protostar and one faint candidate protostar, and the others are categorized as protostars. Megeath et al. (2012) assigned the MIPS magnitudes to IRAC point sources if they were separated by ≤ 2.5 arcsec. Then, we assume that the typical accuracy in the coordinates of the protostars is within 2.5 arcsec. Table 2 lists the properties of protostars and one faint candidate protostar in regions of Figures 2–7. Other names are taken from Evans, Levreault, & Harvey (1986), Anglada et al. (1992), Chini et al. (1997), Lis et al. (1998), Tsuboi, Koyama, Hamaguchi et al. (2001), Takahashi et al. (2009), and Takahashi et al. (2013).

We identified 31 intensity peaks in the CCS $J_N = 7_6 - 6_5$ and/or N_2H^+ $J = 1-0$ $F_1 = 2-1$ emission in the six molecular cloud cores. In Table 3, we list the positions of the detected CCS $J_N = 7_6 - 6_5$ intensity peaks and the line parameters of the CCS spectra measured toward these positions. The peak intensity and linewidth are obtained through Gaussian fitting. The rms noise level is measured for the spectrum binned by 4 channels ($\sim 0.4 \text{ km s}^{-1}$). These local intensity peaks do not necessarily match the original TUKH core position. When a local peak matches the original core position, we use the same name (TUKH021, 097, and 122). We add postfix "A, B, C, ..." after core number TUKH for local intensity peaks different from the original core center position. The NH_3 rotation temperature $T_{rot}(NH_3)$ is taken from Wilson et al. (1999), and then is converted to the gas kinetic temperature T_k by using the formula of Li, Goldsmith, & Menten (2003). The beam size used by Wilson et al. (1999) is 43 arcsec, which is twice as large as our beam. We assume that T_k is constant over intensity peaks in each TUKH region. Li et al. (2013) obtained the distribution of T_k on the basis of their NH_3 map toward the OMC-2/3 region, including the TUKH003 region. The NH_3 cores they identified near TUKH003A-D have $T_k = 14-16$ K. Because their NH_3 cores do not exactly match our CCS $J_N = 7_6 - 6_5$ and N_2H^+ peaks and there is no hint of large T_k variation over TUKH003A–D, we simply use $T_k = 16$ K for all of the TUKH003A–D peaks. It is noted that NH_3 core OriAN-

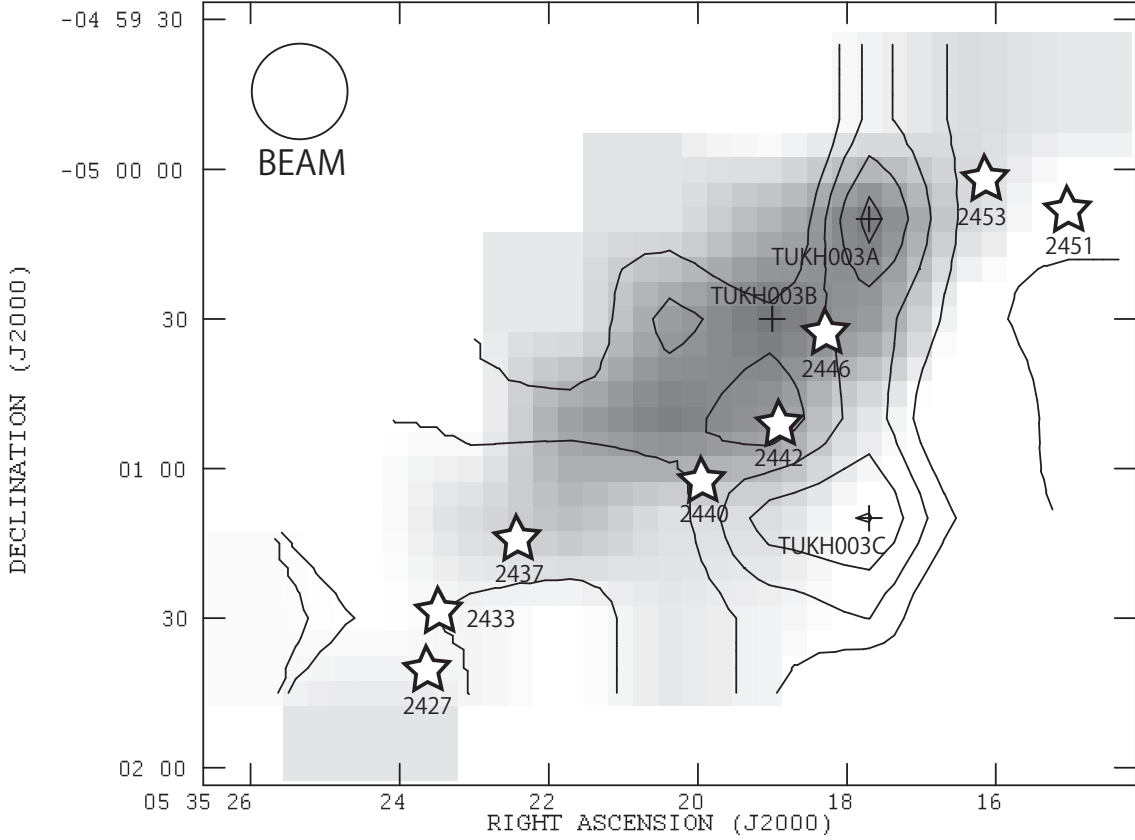


Fig. 2. The CCS $J_N = 7_6 - 6_5$ velocity-integrated intensity map is superimposed on the gray-scale map of the integrated intensity of the main hyperfine component group $N_2H^+ J = 1-0 F_1 = 2-1$ for TUKH003. The velocity range for integration is 9.0 to 13.7 km s^{-1} . The lowest contour is 3σ , and the contour step is 1σ . The 1σ for the contour is 2.7×10^{-2} K km s^{-1} . The maximum in the gray scale corresponds to 5.9 K km s^{-1} . The open star signs represent the location of the protostar in Megeath et al. (2012), and the associated numbers are their identification number. The plus signs represent the location of our cataloged core intensity peak.

535235-50132 at $RA = 5^h 35^m 23^s.5$ $DEC = -5^\circ 01' 32''$ in the TUKH003 region, which does not have $CCS J_N = 7_6 - 6_5$ or N_2H^+ counterpart, has $T_k = 27$ K. Judging from T_k of the six TUKH regions (see Table 3), cores TUKH097 and 117 (and also probably 122) show similar conditions to those found in dark cloud cores. Cores TUKH003, 088, and 021 are warmer than dark cloud cores (with T_k increasing from 16 to 30 K in this order).

We carry out the large velocity gradient (LVG) model by using the RADEX software (Van der Tak et al. 2007) to characterize the $CCS J_N = 7_6 - 6_5$ detected cores. The collision rates for CCS are taken from Wolkovitch et al. (1997). We detected $CCS J_N = 7_6 - 6_5$ at 81.505208 GHz in 7 cores out of the 14 cores toward which $CCS J_N = 4_3 - 3_2$ at 45.379033 GHz was detected. From the LVG analysis, the cores which were not detected in $CCS J_N = 7_6 - 6_5$ are found to have lower densities ($n < 1 \times 10^5 \text{ cm}^{-3}$) than the $CCS J_N = 7_6 - 6_5$ detected cores ($n \gtrsim 1 \times 10^5 \text{ cm}^{-3}$). In the LVG calculations, we assume that the $CCS J_N = 4_3 - 3_2$ and CCS

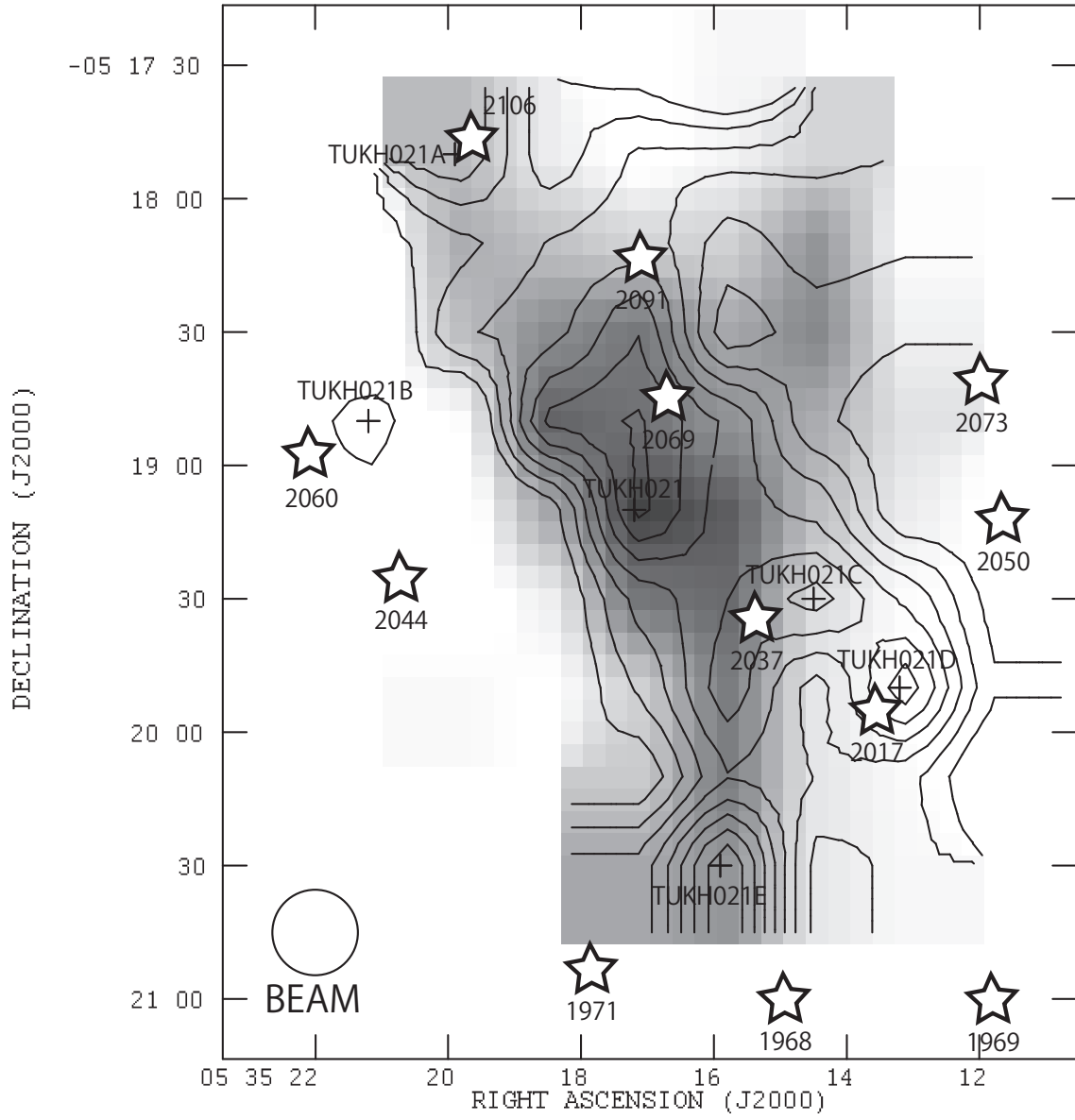


Fig. 3. The same as Figure 2 but for TUKH021. The velocity range for integration is 7.0 to 12.3 km s^{-1} . The 1σ for CCS is $4.6 \times 10^{-2} \text{ K km s}^{-1}$, and the maximum in the gray scale corresponds to 12.5 K km s^{-1} .

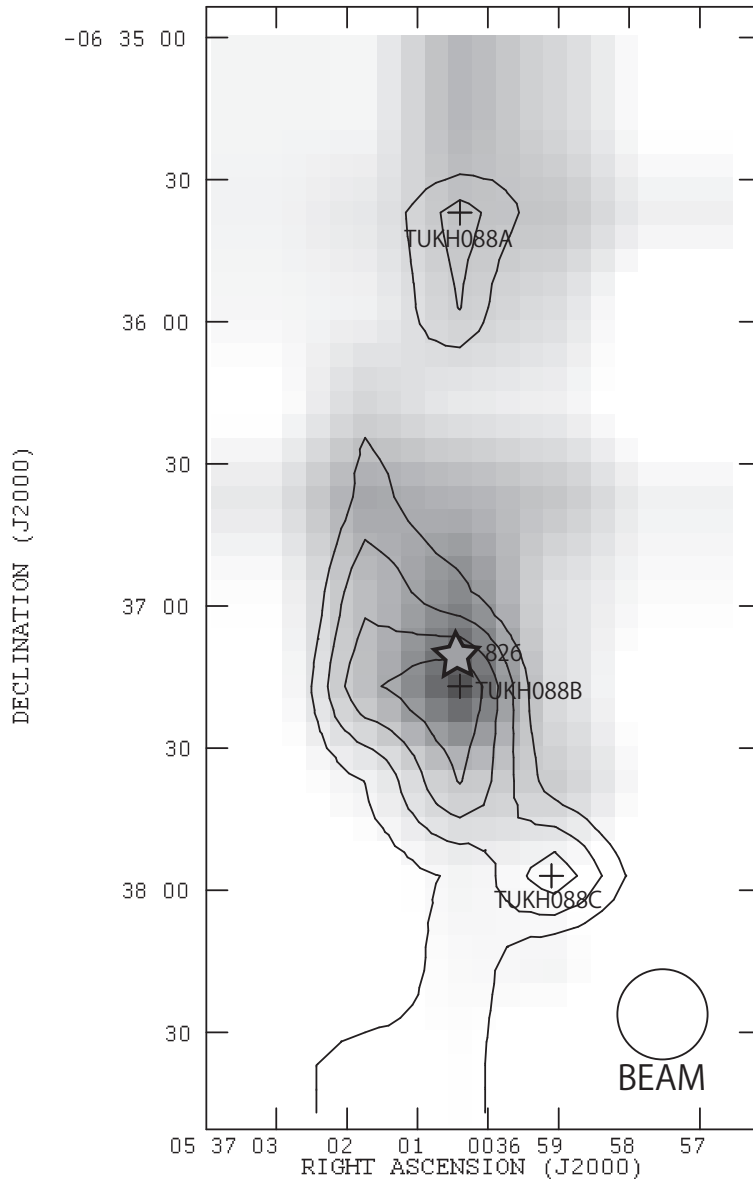


Fig. 4. The same as Figure 2 but for TUKH088. The velocity range for integration is 5.0 to 8.2 km s^{-1} . The 1σ for CCS is $3.4 \times 10^{-2} \text{ K km s}^{-1}$, and the maximum in the gray scale corresponds to 1.33 K km s^{-1} . The gray star sign represents the location of the faint candidate protostar in Megeath et al. (2012).

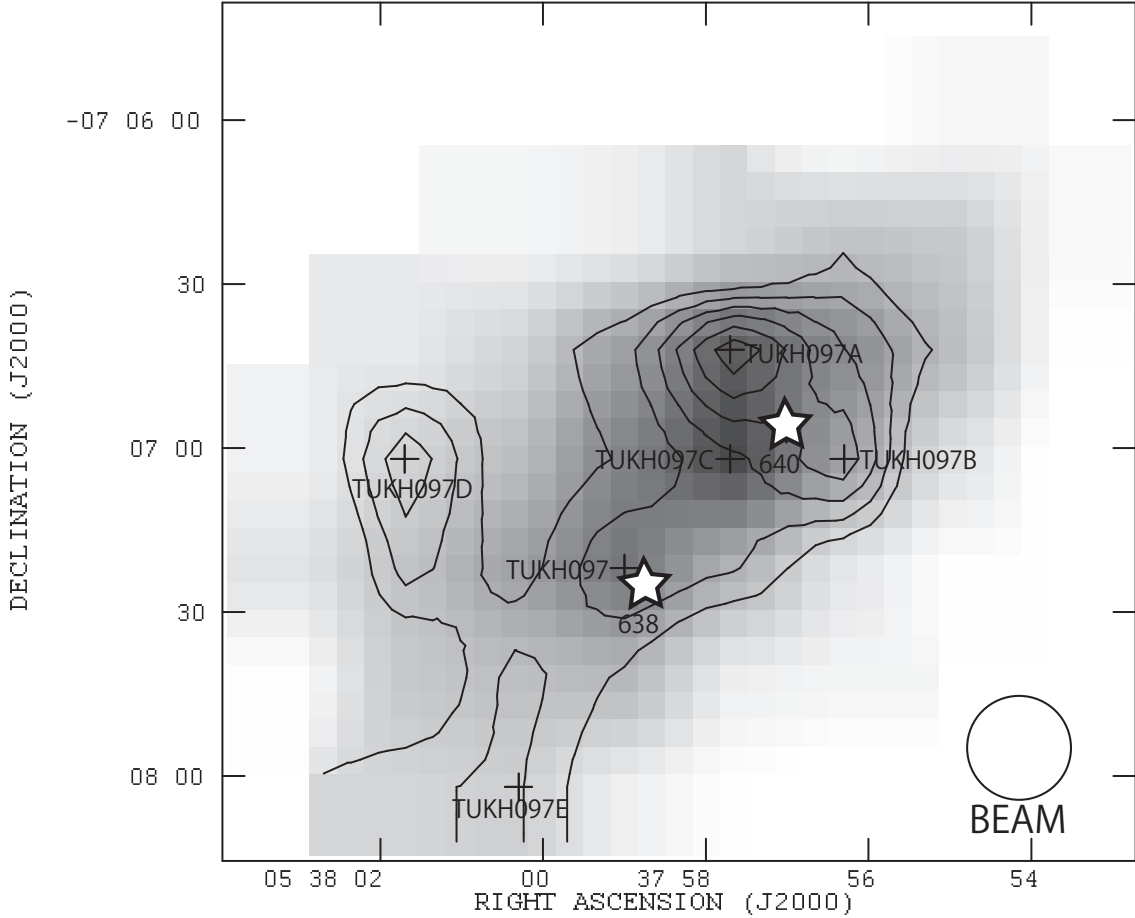


Fig. 5. The same as Figure 2 but for TUKH097. The velocity range for integration is 4.3 to 8.0 km s^{-1} . The 1σ for CCS is 3.1×10^{-2} K km s^{-1} , and the maximum in the gray scale corresponds to 2.75 K km s^{-1} .

$J_N = 7_6 - 6_5$ line emission has similar spatial extent and distribution within the single-dish beam of the observations, and we do not correct for the difference in the beam size. According to Tatematsu et al. (2008), the average density of N_2H^+ $J = 1-0$ cores is of order 1×10^5 cm^{-3} . Then, the CCS $J_N = 7_6 - 6_5$ and N_2H^+ $J = 1-0$ emission seems to trace similar density regions.

In TUKH 088, 097, and 117, there is a trend for the CCS emission to be stronger where the protostar does not exist, while the N_2H^+ $J = 1-0$ $F_1 = 2-1$ emission tends to be stronger toward the protostar (candidate). These tendencies are similar to those found in dark clouds (Benson, Caselli, & Myers 1998). In some cases, the CCS emission is detected toward the protostar as well as the N_2H^+ emission. Note that the N_2H^+ emission is much stronger than the CCS $J_N = 7_6 - 6_5$ emission in general. A possible explanation for the CCS $J_N = 7_6 - 6_5$ emission toward star-forming peaks is that CCS also exists in evolved molecular gas as a secondary late-stage peak due to CO depletion in the chemical evolution (Li et al. 2002 and references therein; Lee et al. 2003).

In the TUKH003 and TUKH021 regions, there are protostars which do not accompany

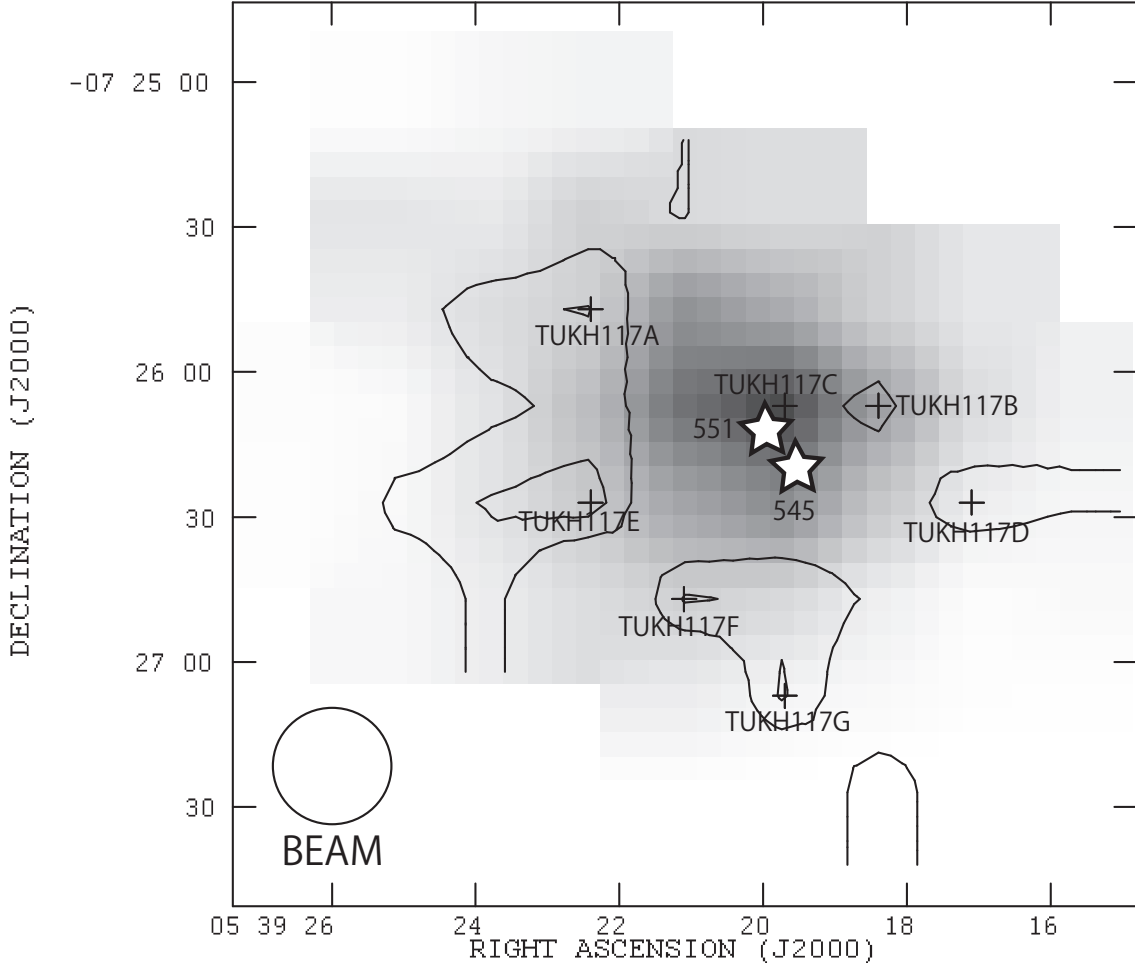


Fig. 6. The same as Figure 2 but for TUKH117. The velocity range for integration is 3.0 to 7.5 km s^{-1} . The 1σ for CCS is 3.7×10^{-2} K km s^{-1} , and the maximum in the gray scale corresponds to 5.06 K km s^{-1} .

the N_2H^+ $J = 1-0$ $F_1 = 2-1$ emission. These are Megeath 2017, 2044, 2050, 2060, 2073, 2091, 2427, 2433, 2437, and 2451. The reason will be investigated in the subsequent subsection.

To see the evolutionary stage of the intensity peaks, we check the association with protostars. We assume that starless intensity peaks are young, while star-forming peaks are more evolved. As a criterion, we classify CCS $J_N = 7_6 - 6_5$ and/or N_2H^+ $J = 1-0$ $F_1 = 2-1$ intensity peaks as “starless” and “star-forming” when the distance between the position of the protostar and the core intensity peak is > 30 arcsec and ≤ 30 arcsec, respectively. We explain why we adopt this criterion. According to Tatematsu et al. (2008) the average radius (half of FWHM) of N_2H^+ $J = 1-0$ cores is 39 ± 12 arcsec. This provides the size scale of the embedded region. Next, we consider the proper motion of the protostar with respect to the parent molecular cloud core after its birth. We take the age of the Class I protostar to be of order $1-3 \times 10^5$ yr (e.g., Greene et al. 1994). We assume that the one-dimensional velocity dispersion (1σ) of the protostar with respect to the core center is equal to that of the velocity

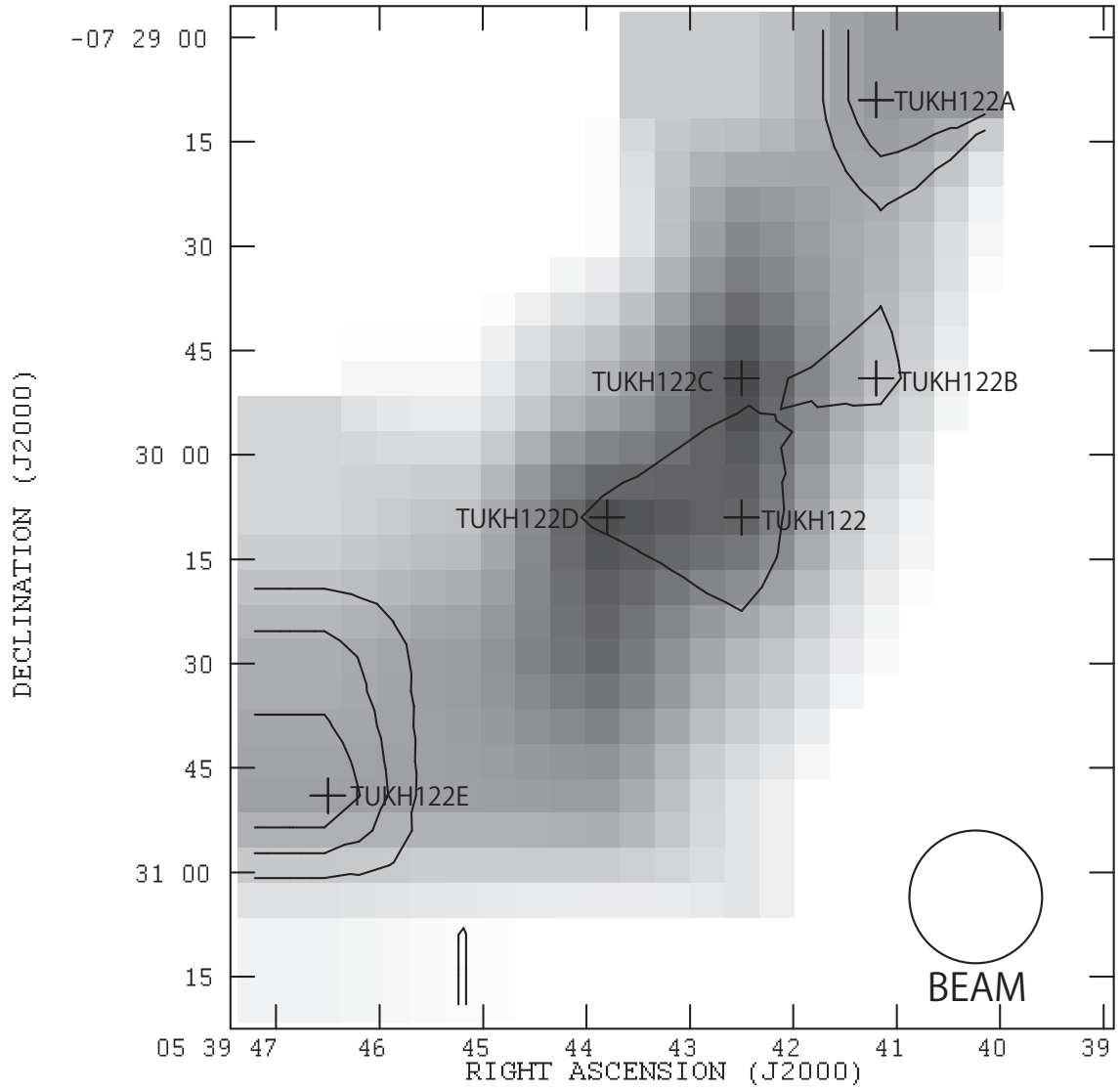


Fig. 7. The same as Figure 2 but for TUKH122. The velocity range for integration is 2.5 to 5.5 km s^{-1} . The 1σ for CCS is $2.8 \times 10^{-2} \text{ K km s}^{-1}$, and the maximum in the gray scale corresponds to 0.88 K km s^{-1} . There is no protostar.

dispersion of the linewidth of the emission toward the core ($\text{FWHM}/(2\sqrt{2\ln 2})$). We take an FWHM linewidth of 0.5 km s^{-1} as a representative number (The FWHM linewidth of N_2H^+ $J = 1-0$ for all the cores except TUKH021 is $0.63\pm 0.23\text{ km s}^{-1}$ as seen from Table 4; to be explained later). Then, the maximum shift perpendicular to the line of sight of the Class I protostar with respect to the core center is 0.07 pc (30 arcsec). Finally, we need take into account the spatial resolution of our observations. Our observations were carried out on a 20 arcsec grid with $19.1\pm 0.3\text{ arcsec}$ beam, and this will determine the positional accuracies of the intensity peaks. Taking these into account, we adopt the criterion of 30 arcsec (0.07 pc) for association with the Spitzer source.

3.2. Individual Regions

In the TUKH003 region (Figure 2), three Spitzer sources are located near N_2H^+ $J = 1-0$ $F_1 = 2-1$ emission. TUKH003B is associated with Megeath 2442 and 2446, which correspond to X-ray emitting protostars TKH10 and TKH8 discovered by Tsuboi, Koyama, Hamaguchi et al. (2001) (see also Tsujimoto et al. 2004), respectively. Tatematsu et al. (2008) observed HC_3N $J = 5-4$ with a 38 arcsec beam and N_2H^+ $J = 1-0$ with a 18 arcsec beam, and found a displacement between the molecular emission from these molecules over 2 arcmin (0.3 pc) scale in this region. The present observations with a 19 arcsec beam show a more complicated distribution. Megeath 2440 is also close to TUKH003B. On the other hand, protostars Megeath 2427, 2433, 2437, and 2451 are not close to any bright CCS $J_N = 7_6 - 6_5$ or N_2H^+ $J = 1-0$ $F_1 = 2-1$ local peaks (i.e., not within a radius of $\leq 30\text{ arcsec}$). Figure 8 compares the CCS $J_N = 7_6 - 6_5$ distribution with the dust continuum emission obtained by Johnstone & Bally (1999) with the James Clerk Maxwell Telescope (JCMT) and the SCUBA (Submillimeter Common-User Bolometer Array). The dust continuum map was obtained with a 14 arcsec beam, which is close to the resolution of our observations. Structures with scales larger than 65 arcsec are missing in their continuum map due to the observing method. The brightest dust continuum source corresponds to MMS6 (Chini et al. 1997), CSO10 (Lis et al. 1998), and OriAN-535235-50132 (Li et al. 2013). Except for this brightest source, the dust continuum distribution is very similar to that of N_2H^+ $J = 1-0$ $F_1 = 2-1$. The N_2H^+ $J = 1-0$ $F_1 = 2-1$ distribution traces relatively well the column density of the high density region affected very little by protostellar feedback, as reported toward low-mass pre-stellar cores (Caselli et al. 1999). However, the brightest dust continuum source OriAN-535235-50132 is associated with molecular gas with $T_k = 27\text{ K}$ (Li et al. 2013), higher than the CO evaporation temperature of CO from the mantles of dust grains at about 25 K (Collings et al. 2004). Therefore, CO evaporated from grain surfaces destroys N_2H^+ significantly in warm regions with $T_{dust} > 25\text{ K}$ (Lee, Bergin, & Evans 2004). Then, it is expected that the N_2H^+ emission is not prominent in warmer regions where stars have already formed. This could be a reason why protostars Megeath 2427, 2433, and 2437 are not associated with N_2H^+ $J = 1-0$ $F_1 = 2-1$ local peaks (see Figure 2).

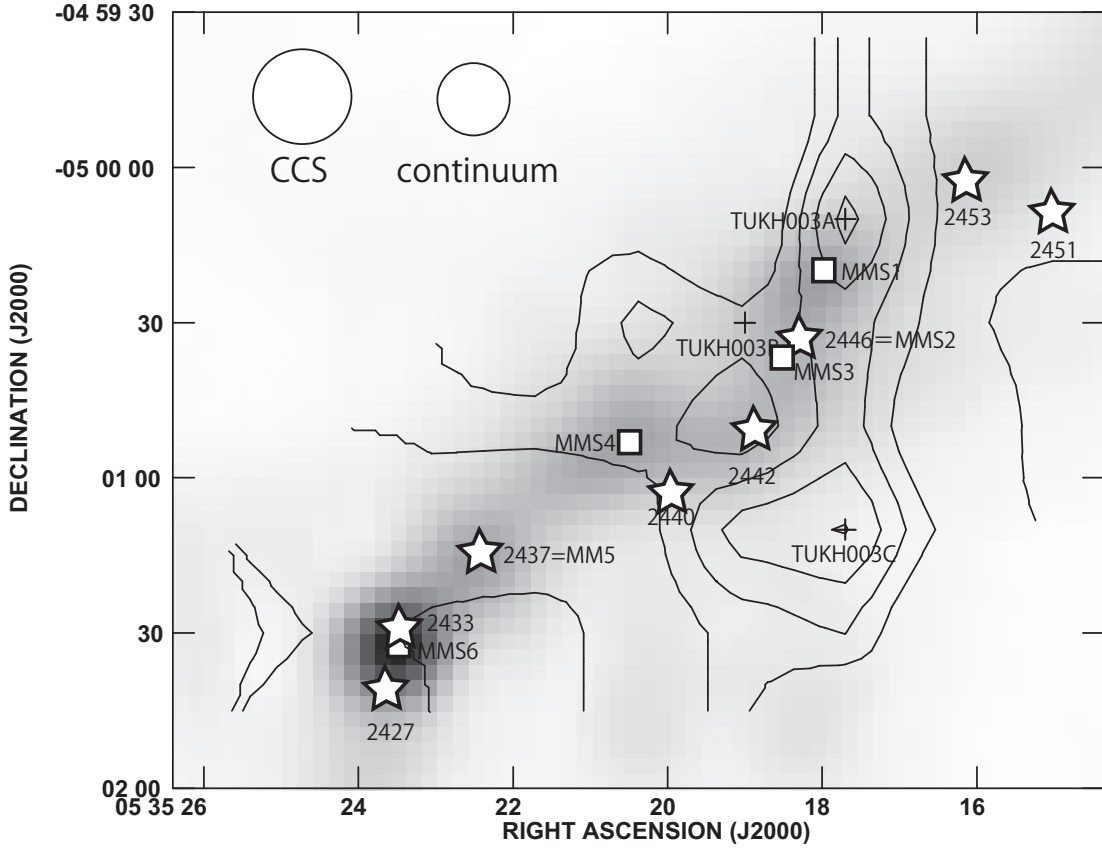


Fig. 8. The CCS $J_N = 7_6 - 6_5$ velocity-integrated intensity map is superimposed on the gray-scale map of the $850 \mu\text{m}$ dust continuum emission of Johnstone & Bally (1999) for TUKH003. The dust continuum map was obtained with a 14 arcsec beam, which is close to the angular resolution of our observations (19 arcsec). Structures with scales larger than 65 arcsec are missing in the continuum map due to the observing technique used (see Johnstone & Bally 1999) The maximum in the gray scale corresponds to 7.4 Jy beam^{-1} . The open box signs represent the 1.3 mm dust continuum sources cataloged by Chini et al. (1997) (source names with the prefix MMS). When the 1.3 mm dust continuum coincides with the protostars, the open box signs are omitted and only the source names are shown.

The TUKH021 region (Figure 3) is located a few arcmin north of Orion KL. There is some correlation between the distribution of CCS $J_N = 7_6 - 6_5$ and N_2H^+ . Megeath 2037, 2069, and 2106 are located near the N_2H^+ $J = 1-0$ $F_1 = 2-1$ emitting regions. On the other hand, protostars Megeath 2017, 2044, 2050, 2073, and 2091 are not close to any of the N_2H^+ $J = 1-0$ $F_1 = 2-1$ local peaks. Megeath 2060 is close to TUKH021B, which is a CCS $J_N = 7_6 - 6_5$ peak. It is not clear whether this is chance coincidence. Figure 9 compares the CCS $J_N = 7_6 - 6_5$ distribution with the dust continuum emission by Johnstone & Bally (1999). Megeath 1971, 2044, and 2060 are located along the south-east dust ridge seen in this figure. Figure 10 compares the CCS $J_N = 7_6 - 6_5$ distribution with the $C^{18}O$ $J = 1-0$ map carried out with the Nobeyama 45 m radio telescope on a 17 arcsec grid with a 15 arcsec beam ². The grid spacing and beam size of the $C^{18}O$ observations are close to those used in the present observations (20 and 19.1 arcsec, respectively). In general, the dust continuum and $C^{18}O$ distribution is more or less similar to the N_2H^+ distribution, but shows appreciable differences from the CCS $J_N = 7_6 - 6_5$ distribution. Warm dust temperature could be a reason why protostars Megeath 2044, 2060, and 2091 are not associated with N_2H^+ $J = 1-0$ $F_1 = 2-1$ local peaks. We adopted the gas kinetic temperature of $T_k = 30$ K obtained toward original core center position TUKH021 (and local intensity peak position) with a 43 arcsec beam, for the overall TUKH021 region. Judging from Figure 8 of Wiseman & Ho (1998), whose spatial resolution is 8.5×9.0 arcsec, the gas kinetic temperature T_k changes in a complicated way from 18 to 45 K between $DEC(J2000.0) = -05^\circ 20' 00''$ and $-05^\circ 19' 00''$. It seems that this region has small-scale gas kinetic temperature variations. Since we do not have gas kinetic temperature measurements which exactly match our beam and sampling, it is hard to assign the gas kinetic temperature to each local intensity peak. The excitation temperature of N_2H^+ toward TUKH021 is 20.8 ± 1.8 K. Then, the gas kinetic temperature T_k toward TUKH021 with a 19 arcsec beam will be > 21 K.

In the TUKH088 region (Figure 4), faint candidate protostar Megeath 826 is associated with TUKH088B, where both the N_2H^+ $J = 1-0$ $F_1 = 2-1$ and CCS $J_N = 7_6 - 6_5$ intensity peaks are detected. The CCS $J_N = 7_6 - 6_5$ emission is extended toward the south, where no protostar is found. In the north, there is one CCS $J_N = 7_6 - 6_5$ intensity peak without a protostar.

In the TUKH097 region (Figure 5), two protostars, Megeath 638 and 640, are associated with local peaks of the N_2H^+ $J = 1-0$ $F_1 = 2-1$ emission, TUKH097, TUKH097A, and TUKH097B, when we adopt the 30 arcsec criterion. It seems the CCS $J_N = 7_6 - 6_5$ emission is also peaked near these two protostars. We found two other CCS intensity peaks, TUKH097D and TUKH097E (for TUKH097E, contours are not closed due to the limited observed area), which are not associated with protostars.

The TUKH117 region (Figure 6) is associated with Haro 4-255 FIR, which drives a

² The data available at <http://alma.mtk.nao.ac.jp/~kt/fits.html>

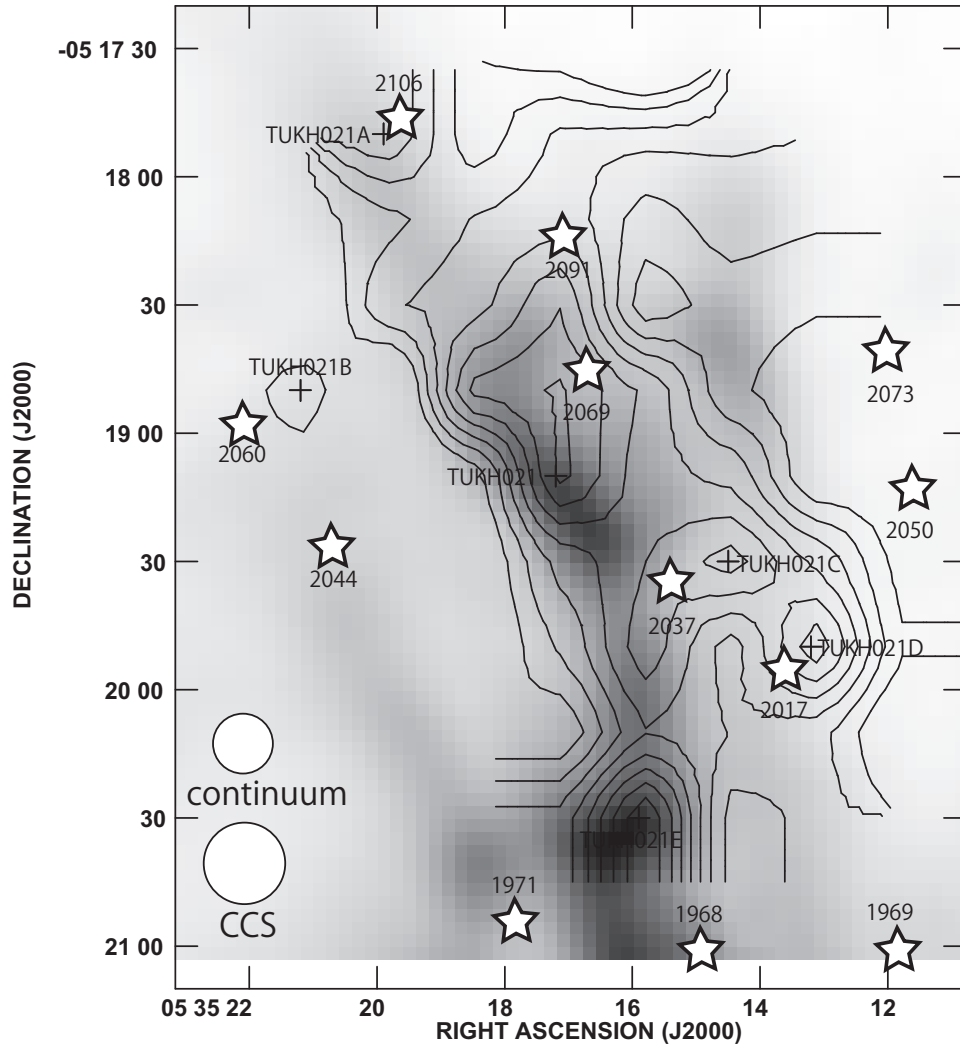


Fig. 9. The same as Figure 8 but for TUKH021. The maximum in the gray scale corresponds to $11.7 \text{ Jy beam}^{-1}$.

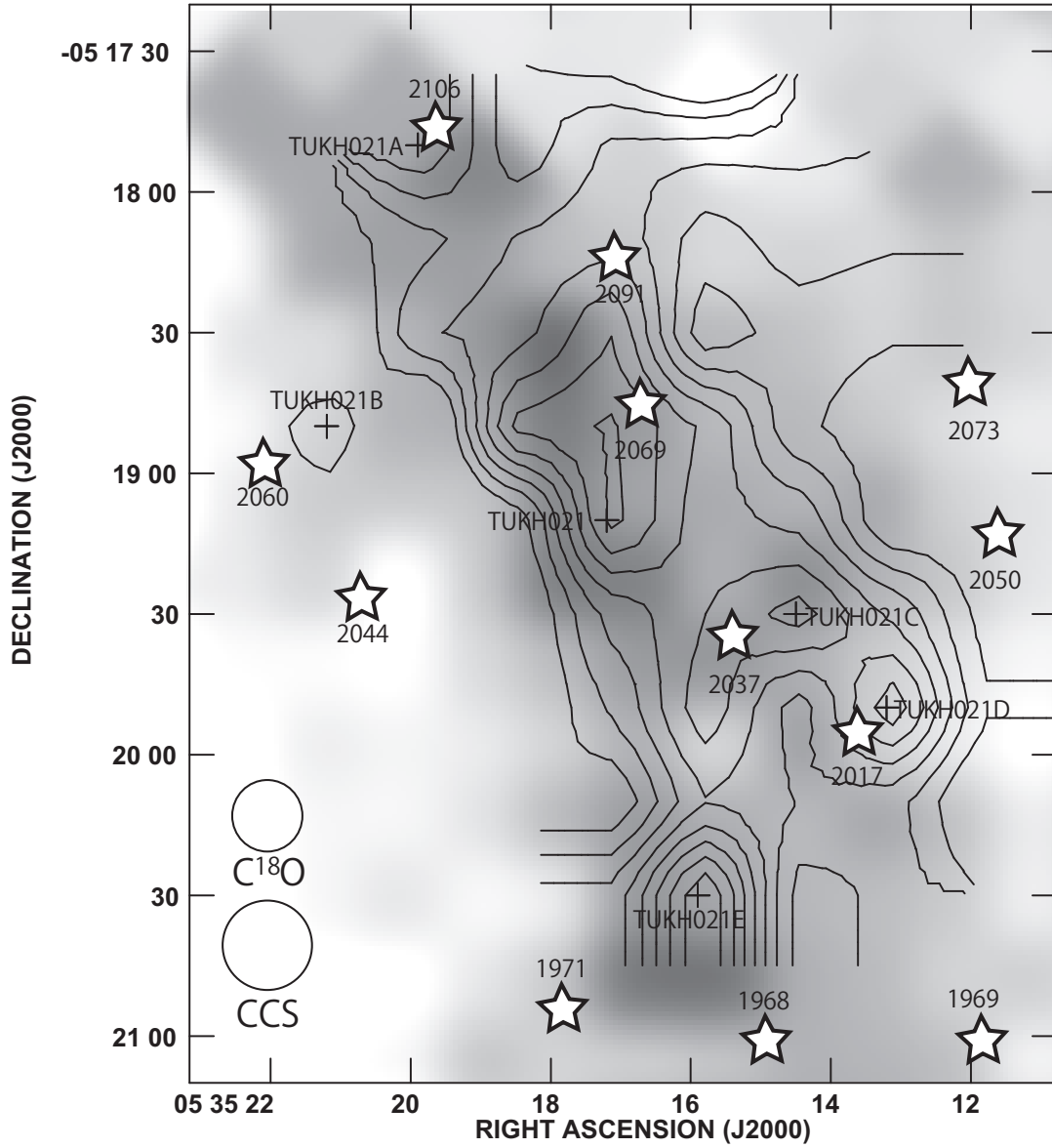


Fig. 10. The CCS $J_N = 7_6 - 6_5$ velocity-integrated intensity map is superimposed on the gray-scale map of C¹⁸O $J = 1-0$ for TUKH021. The C¹⁸O data were obtained on a 17 arcsec grid with a 15 arcsec beam. The velocity range for C¹⁸O is 5.0 to 13.7 km s⁻¹. The maximum in the gray scale corresponds to 5.1 K km s⁻¹.

molecular outflow (Evans, Levreault, & Harvey 1986; Levreault et al. 1988), and with the VLA point source Haro 4-255 VLA1 (Anglada et al. 1992). It is likely that Megeath 545 and 551 correspond to Haro 4-255 VLA1 and Haro 4-255 FIR, respectively. The N_2H^+ $J = 1-0$ $F_1 = 2-1$ emission is distributed around these two Spitzer sources. It is found that the CCS $J_N = 7_6 - 6_5$ and N_2H^+ distribution are anticorrelated. This is consistent with the tendency found in dark clouds (Aikawa et al. 2001). The CCS $J_N = 7_6 - 6_5$ and N_2H^+ $J = 1-0$ $F_1 = 2-1$ distribution in the present observation roughly correspond to the C^{18}O and NH_3 distribution in low-resolution maps summarized in Tatematsu et al. (1993b), respectively.

The TUKH122 region (Figure 7) is starless. In Tatematsu et al. (2010), TUKH122 is the most CCS $J_N = 4_3 - 3_2$ intense core, although the CCS column density is close to the average obtained from the CCS $J_N = 4_3 - 3_2$ detected cores. The N_2H^+ $J = 1-0$ $F_1 = 2-1$ and CCS $J_N = 7_6 - 6_5$ intensity peaks are located within 1 arcmin region near the map center. It is most likely that this 1 arcmin region represents a physical density peak, because these molecules, which sometimes show different distribution suggesting the chemical evolution, coexist in the 1 arcmin region. The LTE mass and virial mass of the core are estimated to be 49 and 26 M_\odot , respectively, from CS $J = 1-0$ observations (Tatematsu et al. 1993a). Because we detected the emission from the late-type molecule N_2H^+ and there is no protostar, it is possible that the TUKH122 region is on the verge of star formation (cf. Caselli et al. 1999).

3.3. *Hyperfine Line Fitting, Integrated Intensity Ratios, and Column Density Ratios*

We fit the hyperfine component model to the N_2H^+ $J = 1-0$ spectrum, and derive the optical depth, LSR velocity, linewidth, and excitation temperature. The intrinsic line strength of the hyperfine components is adopted from Tiné et al. (2000). The results are shown in Table 4. The optical depth τ_{TOT} is the sum of the optical depths of all the hyperfine components. The velocity-integrated intensity $W = \int T_A^* dv$ of the main hyperfine component group N_2H^+ $J = 1-0$ $F_1 = 2-1$ is also listed. Blank cells represent that the hyperfine line fitting is not successful or that derived parameters have too large fitting errors. Figures 11 to 17 show some examples with the results of hyperfine line fitting method. In some cases, the hyperfine line fitting is not very good, because regions contain two velocity components or skewed velocity profiles. We have also tried two velocity component fitting, which provides us with better fitting. On the other hand, two velocity component Gaussian fitting to the CCS spectrum is hard to carry out because of lower signal-to-noise ratios in the CCS spectrum. There is no guarantee that the CCS emission has the same velocity components as the N_2H^+ emission. Because the main purpose of the present study is a comparison of the CCS and N_2H^+ emission, we adopt the single-velocity hyperfine line fitting in this paper. The N_2H^+ LSR velocity from single-velocity fitting is more consistent with the CCS LSR velocity than the N_2H^+ LSR velocities from two-velocity fitting. For example, TUKH003B has an N_2H^+ and CCS velocity of 11.05 and 10.98 km s^{-1} , respectively, while the two-velocity fitting for N_2H^+ gives 10.58 and 11.18 km s^{-1} . In

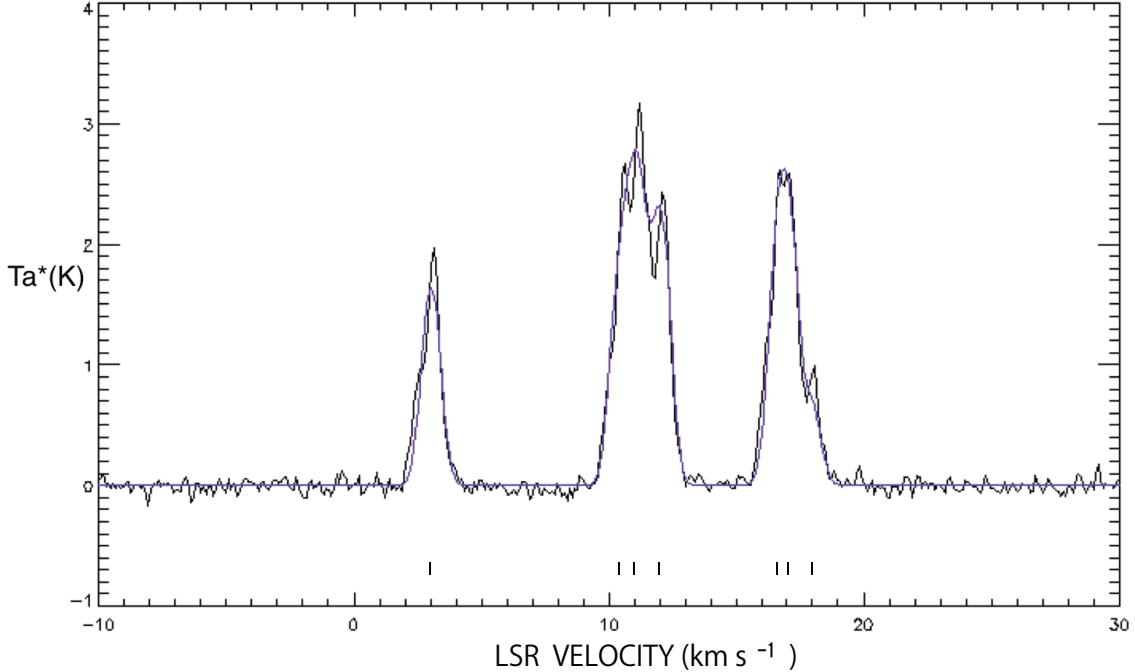


Fig. 11. Hyperfine line fitting result for the N_2H^+ $J = 1-0$ spectrum for TUKH003B. Seven short vertical bars are shown to illustrate the velocity offset corresponding to the frequency offset of the hyperfine components.

our future, separate paper, we plan to investigate the core dynamics on the basis of the N_2H^+ spectra and the result of multi-velocity-component hyperfine line fitting will be presented there.

Figure 18 compares the excitation temperature T_{ex} derived from the N_2H^+ $J = 1-0$ hyperfine line fitting method against T_k derived from NH_3 (Wilson et al. 1999). The open circle and filled circle represent star forming and starless peaks, respectively. When the emission is more optically thin, we cannot constrain the optical depth well and the error bars are large (one core at $T_k = 29$ K has $\tau_{TOT} = 0.7 \pm 0.5$ and τ for each component is 0.1–0.2). In general, T_{ex} (N_2H^+) is appreciably lower than T_k . We conclude that the N_2H^+ $J = 1-0$ levels are only subthermally excited.

In Figure 19, the ratio of the velocity-integrated intensity of the N_2H^+ main hyperfine group $J = 1-0$ $F_1 = 2-1$ to that of the CCS $J_N = 7_6 - 6_5$ emission is plotted against T_k . It seems that star forming peaks tend to have larger ratios.

Next, we compare the column density of N_2H^+ with that of CCS. The column density is calculated by assuming local thermodynamic equilibrium (LTE). The formulation can be found, for example, in Suzuki et al. (1992). We use the N_2H^+ line parameters derived from the hyperfine line fitting method. The excitation temperature T_{ex} (CCS) is assumed to be equal to that for N_2H^+ when the hyperfine line fitting to the N_2H^+ $J = 1-0$ spectrum at the same position is successful. In some cases, LSR velocities of the N_2H^+ $J = 1-0$ and CCS $J_N = 7_6 - 6_5$ emission at the same position differ slightly, which means that emitting regions are

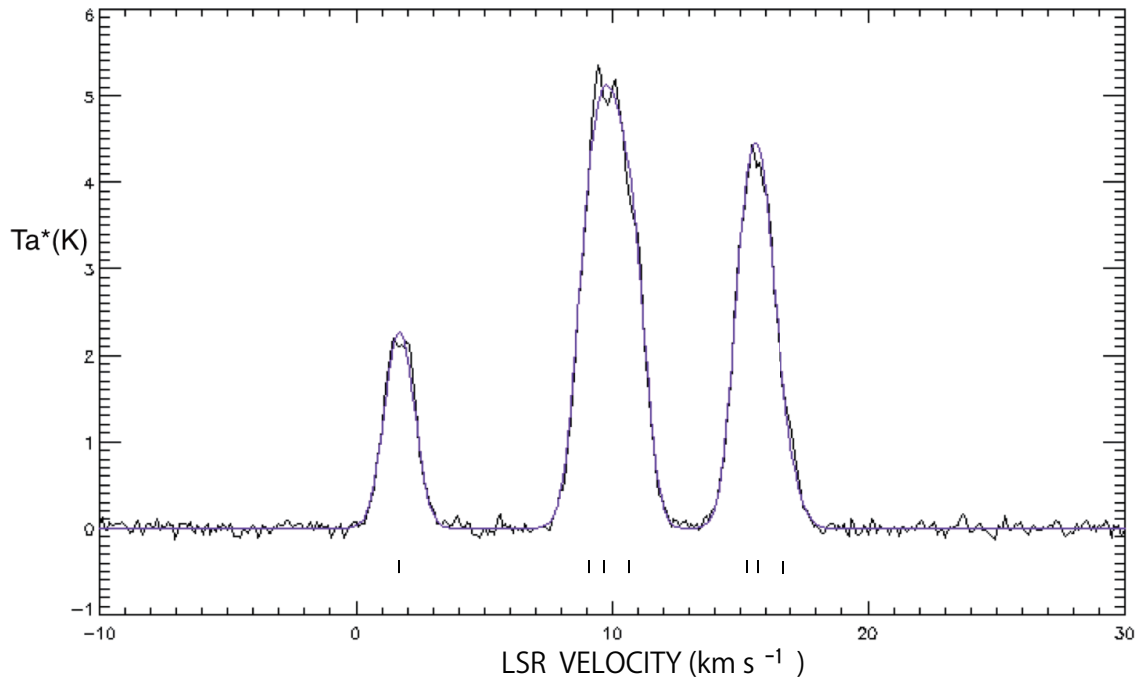


Fig. 12. The same as Figure 11 but for TUKH021.

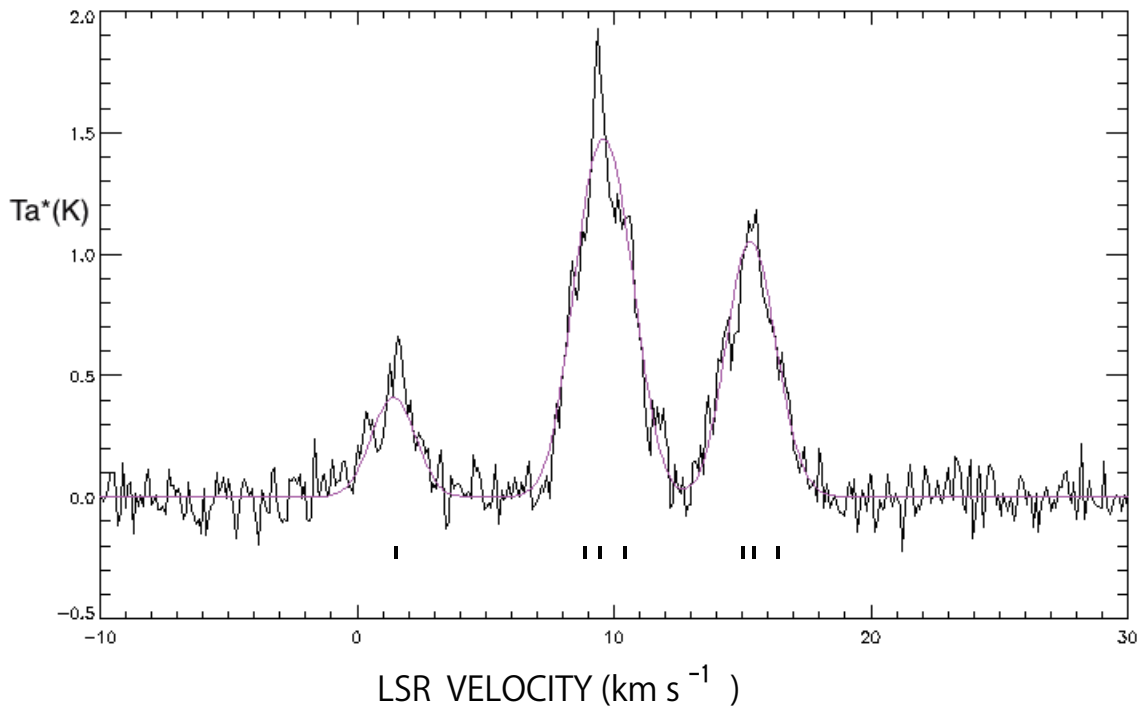


Fig. 13. The same as Figure 11 but for TUKH021C.

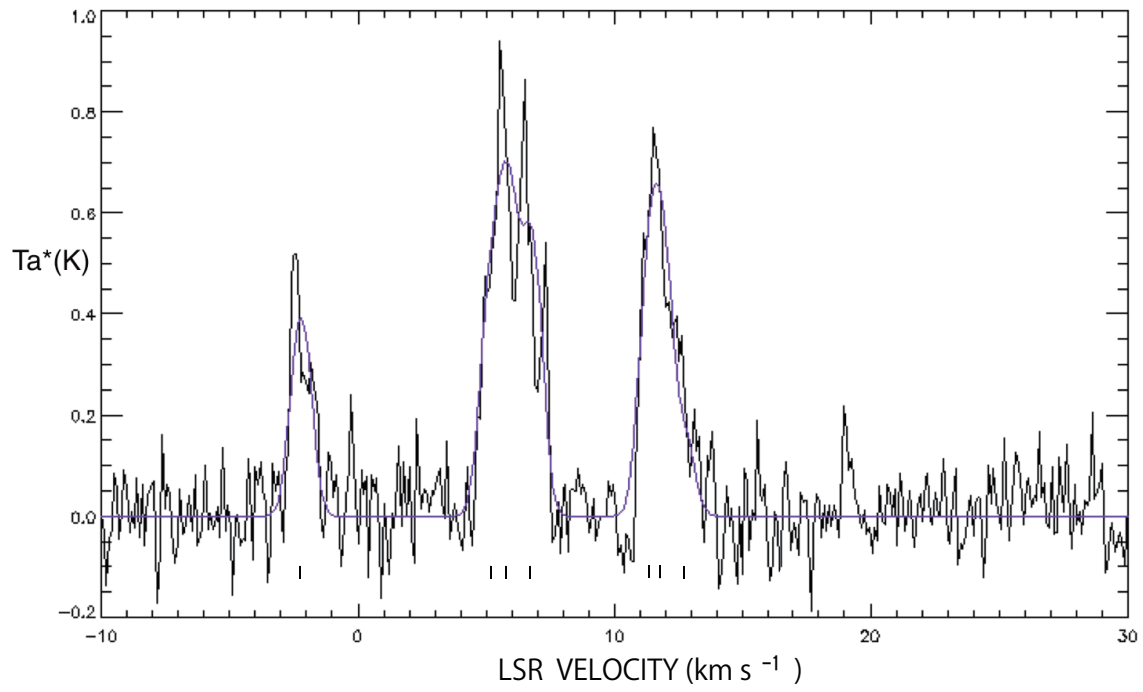


Fig. 14. The same as Figure 11 but for TUKH088B.

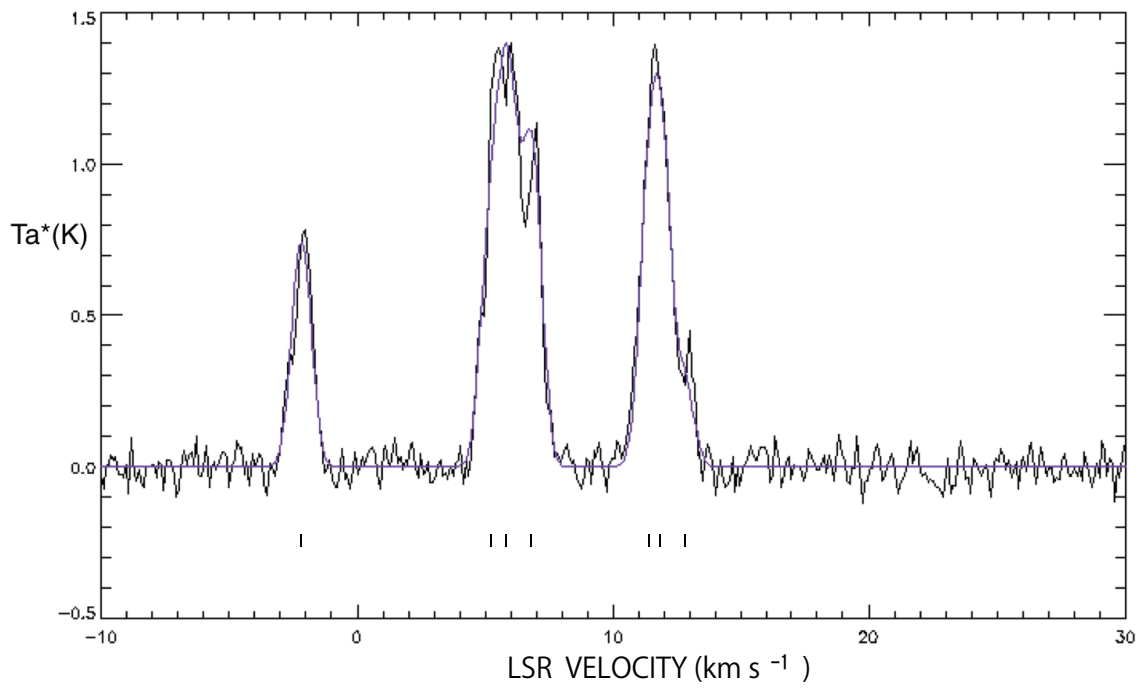


Fig. 15. The same as Figure 11 but for TUKH097C.

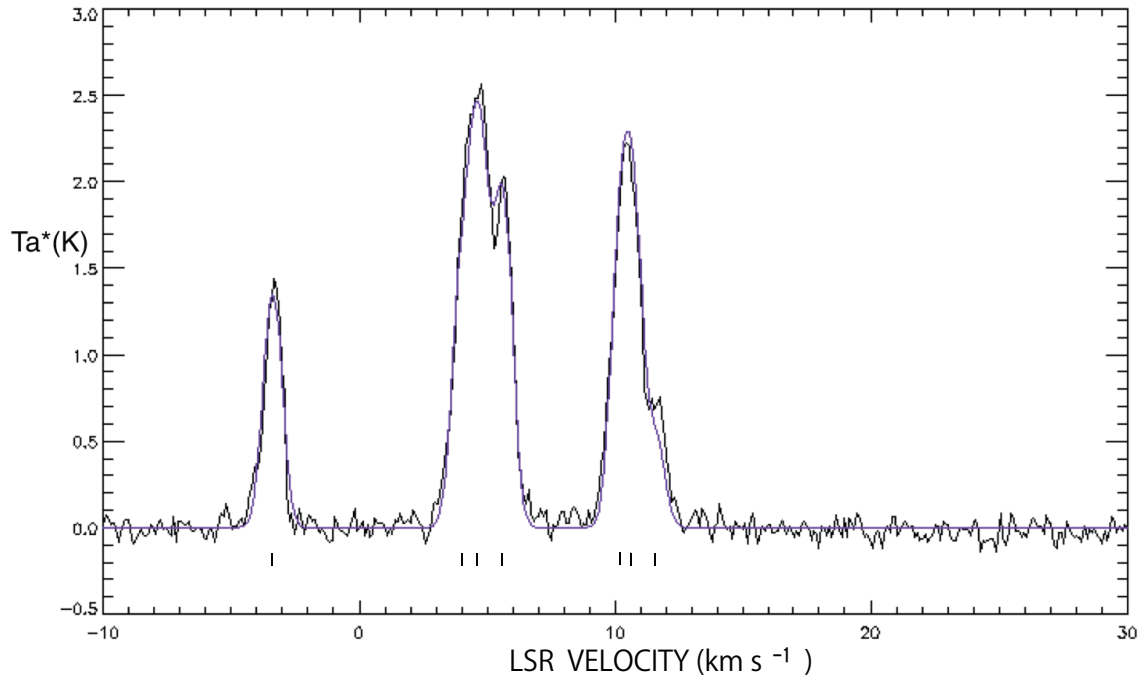


Fig. 16. The same as Figure 11 but for TUKH117B.

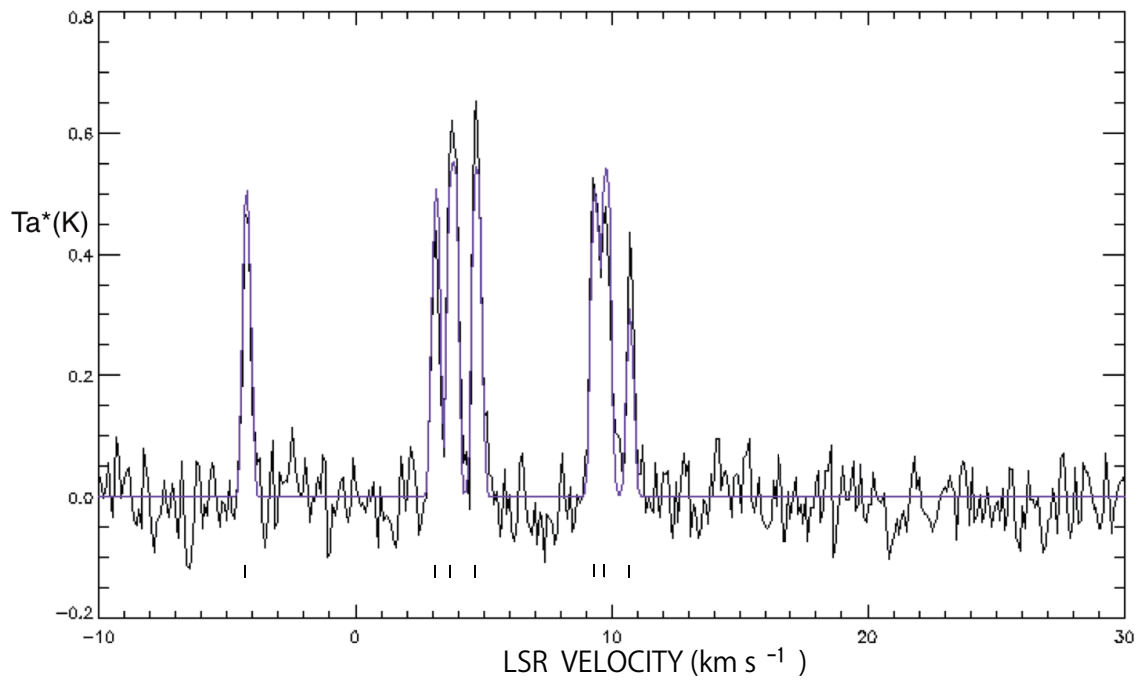


Fig. 17. The same as Figure 11 but for TUKH122.

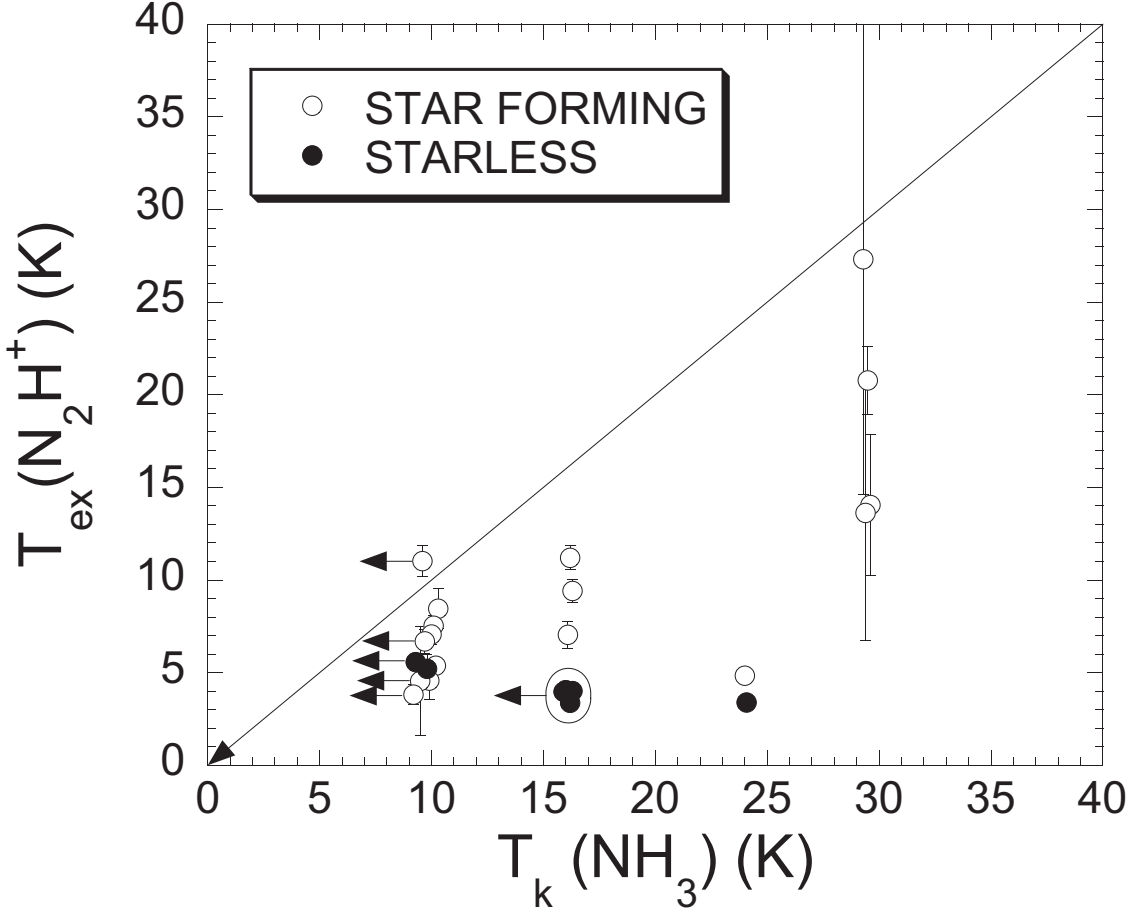


Fig. 18. The N_2H^+ $J = 1-0$ excitation temperature is plotted against the gas kinetic temperature T_k . The gas kinetic temperature is obtained from the NH_3 rotation temperature in Wilson et al. (1999) with the conversion formula of Li, Goldsmith, & Menten (2003). The horizontal arrow represents the upper limit to T_k . The vertical error bar represents the 1σ error corresponding to the line optical depth in the N_2H^+ $J = 1-0$ hyperfine line fitting. Circles are slightly shifted so that error bars do not overlap with each other. The straight line $T_{ex} = T_k$ is shown.

different. Even in such cases, we simply assume the same excitation temperature as a best guess. When the hyperfine line fitting is not successful due to low signal to noise ratios, we adopt $T_{ex}(\text{CCS}) = T_k(\text{NH}_3)/2$ (when Wilson et al. 1999 provide the upper limit to T_{rot} , we simply adopt this upper limit value). In one case, the error bar is large. This comes from a large error in the N_2H^+ optical depth because the optical depth is thin (one core at $T_k = 29$ K has $\tau_{TOT} = 0.7 \pm 0.5$ and τ for each component is $0.1-0.2$). Table 5 summarizes the derived column densities. Blank cells indicate that column densities could not be determined due to the low signal-to-noise ratio in the N_2H^+ $J = 1-0$ spectra. Figure 20 shows the ratio of the column density of N_2H^+ to that of CCS against T_k . The number of points in Figure 20 is smaller than that in Figure 19, because in some cases hyperfine line fitting is not successful and we cannot obtain the N_2H^+ column density. One circle at $T_k = 29$ K has a very large error bar,

because the spectrum is close to optically thin limit and the optical depth cannot be constrained precisely. It is found that the column density ratio of $N(\text{N}_2\text{H}^+)/N(\text{CCS})$ is low toward starless peaks while it is high toward star-forming peaks. This is very similar to the tendency found in dark clouds ($T_k \sim 10$ K) Benson, Caselli, & Myers (1998). The criterion found in the Orion A GMC is $N(\text{N}_2\text{H}^+)/N(\text{CCS}) \sim 2 - 3$. That is, $N(\text{N}_2\text{H}^+)/N(\text{CCS})$ is $\lesssim 2 - 3$ in starless peaks, and $\gtrsim 2 - 3$ in star-forming peaks. TUKH097E, 117F, 122C, 122, and 122D have larger column density ratios among starless peaks, and their values are close to the criterion of $2 - 3$ between starless and star-forming peaks found in the present study. It is possible that these represent the sites for near future star formation. TUKH122C, 122, and 122D are of particular interest, because the TUKH122 region does not have any protostar and shows the narrowest N_2H^+ line profiles found in our sample. The non-thermal contribution to the CCS and N_2H^+ lines lies below the sonic value, implying that the cores are mainly thermally supported. The observed CCS and N_2H^+ linewidth are 0.27–0.39 and 0.27–0.28 km s^{-1} , respectively. The thermal linewidth corresponding to 10 K for the mean molecular weight (2.33 a.m.u.) is 0.44 km s^{-1} . Then, the observed linewidth is subsonic. When we adopt the definition of Myers (1983), the non-thermal (turbulent) linewidth Δv (turb) is 0.25–0.38 and 0.24–0.25 km s^{-1} for CCS and N_2H^+ , respectively.

Figure 20 shows that there is no or a weak anticorrelation between T_k and $N(\text{N}_2\text{H}^+)/N(\text{CCS})$. Some may think that $N(\text{N}_2\text{H}^+)/N(\text{CCS})$ has no correlation with T_k , while others may think that $N(\text{N}_2\text{H}^+)/N(\text{CCS})$ is weakly anticorrelated with T_k . Figure 19 shows similar relationship between T_k and $W(\text{N}_2\text{H}^+)/W(\text{CCS})$. Tatematsu et al. (2010) found that $N(\text{NH}_3)/N(\text{CCS})$ decreases with increasing T_{rot} . $N(\text{NH}_3)/N(\text{CCS})$ ranges from ~ 3 to ~ 100 in their study. Marka et al. (2012) investigated the time evolution of the CCS and NH_3 abundances through the chemical model calculations with different kinetic temperatures of 10, 15 and 25 K. Their Figure 5 shows that the CCS abundance increases with increasing kinetic temperature, at a given time. The CCS abundance for 25 K is about a factor of 5 higher than that for 10 K, for $1-3 \times 10^4$ yr. However, For $> 3 \times 10^4$ yr, the abundance difference for 10–25 K becomes complicated. The NH_3 abundance does not show simple increase or decrease with increasing kinetic temperature. We wonder if there is a tendency that the CCS abundance increases with increasing kinetic temperature. Figure 21 shows the NH_3 and CCS abundances against T_K on the basis of Wilson et al. (1999) and Tatematsu et al. (2010). We used $N(\text{H}_2)$ from C^{18}O 2–1 by Wilson et al. (1999). The CCS abundance is almost constant against T_k , while the NH_3 abundance decreases with increasing T_k . When we use the CS column density from CS 1–0 as reference for abundance, we see similar tendencies (not shown). Therefore, observationally, we do not see evidence of $N(\text{CCS})$ increase with increasing T_k . For warm regions ($T_{dust} \gtrsim 25$ K), the abundance of N_2H^+ is expected to be lower for higher T_k since CO evaporates from the mantles of dust grains. The dust temperature T_{dust} and the gas kinetic temperature T_k can be different from each other, but may have some similarity. Then, in warm region ($T_k \gtrsim 25$ K),

the N_2H^+ abundance can be decreased. This could be a reason why Figure 20 shows that there can be a weak anticorrelation between T_k and $N(\text{N}_2\text{H}^+)/N(\text{CCS})$.

Tatematsu et al. (2010) stated that the ratio of the column density of NH_3 to that of CCS in the Orion A GMC is not necessarily high toward star-forming cores. The column density ratio ranges from 6 to 200 when T_{ex} (CCS) is assumed to be $T_{rot}(\text{NH}_3)/2$. Because the CCS $J_N = 4_3 - 3_2$ observations by Tatematsu et al. (2010) were single-point observations toward the core center, and also because the spatial resolution in CCS $J_N = 4_3 - 3_2$ was twice worse than our current CCS $J_N = 7_6 - 6_5$ observations, the identification of starless and star-forming cores was not accurate enough.

Sakai, Oka, & Yamamoto (2006) and Sakai, Oka, & Yamamoto (2007) observed W3 GMC including AFGL 333 in CCS $J_N = 4_3 - 3_2$, NH_3 , N_2H^+ , and other lines. They detected the CCS emission in two clumps in AFGL 333, and found that $N(\text{N}_2\text{H}^+)/N(\text{CCS})$ is low (0.5–1.7) in starless clump B and high (2–5) star-forming clump A. Our result based on a larger sample of cores is consistent with their result in W3 GMC. Sakai et al. (2008) observed IRDC (Infrared Dark Clouds) in CCS $J_N = 4_3 - 3_2$, NH_3 , N_2H^+ , and other lines, and did not detect CCS $J_N = 4_3 - 3_2$ in any objects. The lower limit to $N(\text{N}_2\text{H}^+)/N(\text{CCS})$ in IRDCs is mostly $\gtrsim 2$, judging from their sensitivity limit. They concluded that IRDCs are more evolved than nearby dark clouds. Sanhueza et al. (2012) studied IRDCs in N_2H^+ , CCH and HC_3N , and other molecular species. They found that the total column densities of the different molecules, except CCH, increase with the evolutionary stage of the clumps. Their observations did not include CCS lines. According to the production mechanism of CCS proposed by Suzuki et al. (1992), a reaction of CCH with S^+ is a major route to produce CCS. Beuther et al. (2008) has shown that CCH is a tracer of young molecular gas. Although CCS has not been observed in IRDCs yet, it can be just due to lower sensitivity. Tatematsu et al. (2010) compared their detection limit with that in Sakai et al. (2008). Note that Tatematsu et al. (2008) did not detect CCS $J_N = 4_3 - 3_2$ but Tatematsu et al. (2010) did with better sensitivity, in the Orion A GMC. The CCH column density does not show large variations among IRDCs in Sanhueza et al. (2012). If the production mechanism of CCS proposed by Suzuki et al. (1992) is valid for IRDCs, CCS is also expected to vary little across this IRDCs sample. CCS observations toward IRDCs will let us compare the CCH and CCS abundance, and tell us how CCS forms in IRDCs.

According to Benson, Caselli, & Myers (1998), $N(\text{N}_2\text{H}^+)/N(\text{CCS})$ ranges from 0.3 to 3.3 in dark clouds. The column density ratio we derived ranges from 0.3 to 70, and the span is larger. This may be due to the fact that Orion A GMC presents larger chemical variations than those seen in dark clouds, which can be a consequence of the expected differences produced by larger variations in the kinetic temperature of the gas in the Orion A GMC (see Marka et al. 2012).

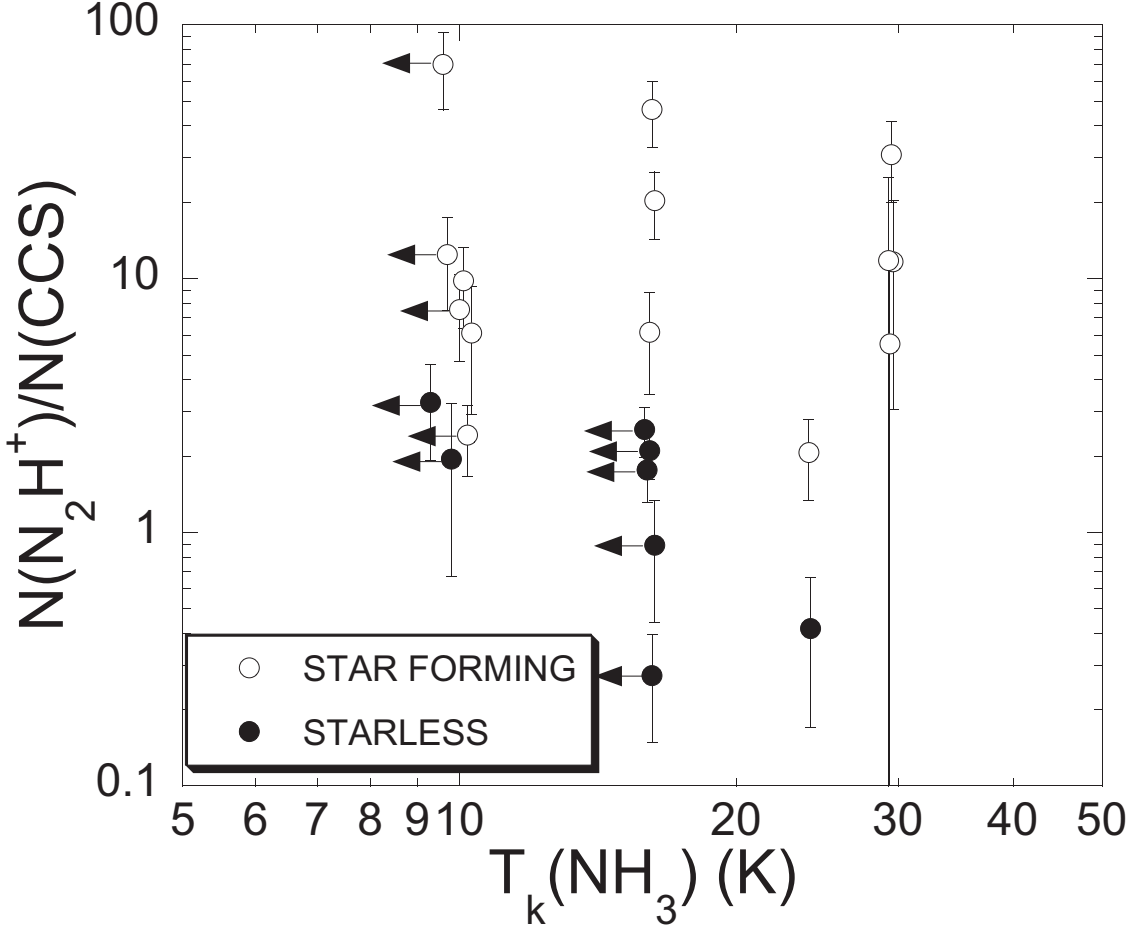


Fig. 20. The ratio of the column density of N_2H^+ to that of CCS is plotted against the gas kinetic temperature T_k . The error bar represent the 1σ error in the optical depth only in the N_2H^+ hyperfine line fitting.

3.4. Validity of our results against the optical depth of the CCS lines

To estimate a typical optical depth of the CCS $J_N = 7_6 - 6_5$ emission, we carry out the large velocity gradient (LVG) model again. We take TUKH122 as an example having low kinetic temperature, large molecular column density, and narrow linewidth. In CCS $J_N = 4_3 - 3_2$ at 45.379033 GHz, the intensity is $T_A^* = 0.47$ K ($T_R = 0.64$ K) and the linewidth is 0.55 km s^{-1} . In CCS $J_N = 7_6 - 6_5$ at 81.505208 GHz, the intensity is $T_A^* = 0.36$ K ($T_R = 0.88$ K) and the linewidth is 0.27 km s^{-1} . We assumed the common linewidth of 0.4 km s^{-1} for LVG models. Although the FWHM used in observations differs between CCS $J_N = 4_3 - 3_2$ at 45.379033 GHz (FWHM beam size = 39 arcsec) and CCS $J_N = 7_6 - 6_5$ at 81.505208 GHz (19 arcsec), we simply compare the intensities without any correction for different beam sizes. The observations and models are listed in Table 6. ‘‘Observation’’ represents the value obtained at TUKH122. ‘‘Model’’ represents the best fit models. ‘‘(Model)’’ represents models with the CCS column density obtained from the LTE calculation for the CCS $J_N = 7_6 - 6_5$

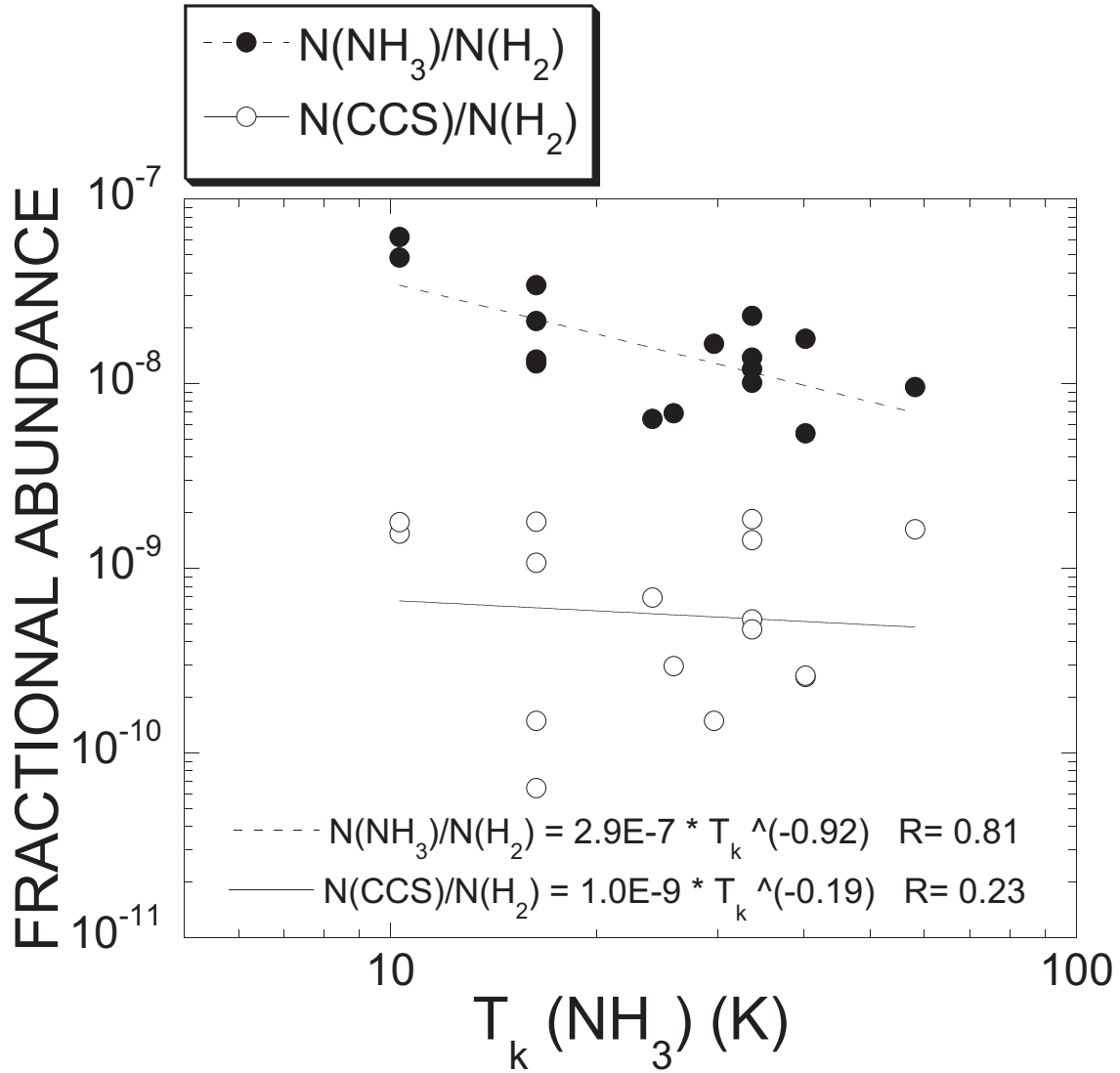


Fig. 21. Fractional abundances of NH_3 and CCS are plotted against the kinetic temperature T_k . Fractional abundances are obtained from the ratio of column densities to $N(\text{H}_2)$. The NH_3 data and $N(\text{H}_2)$, which was obtained from C^{18}O 2-1 data, are taken from Wilson et al. (1999). The CCS column density is taken from Tatematsu et al. (2010), and here we adopt values obtained by assuming $T_{ex} = T_{rot}/2$. We used only cores which were detected in $\text{CCS } J_N = 4_3 - 3_2$ and also have T_{rot} measurements.

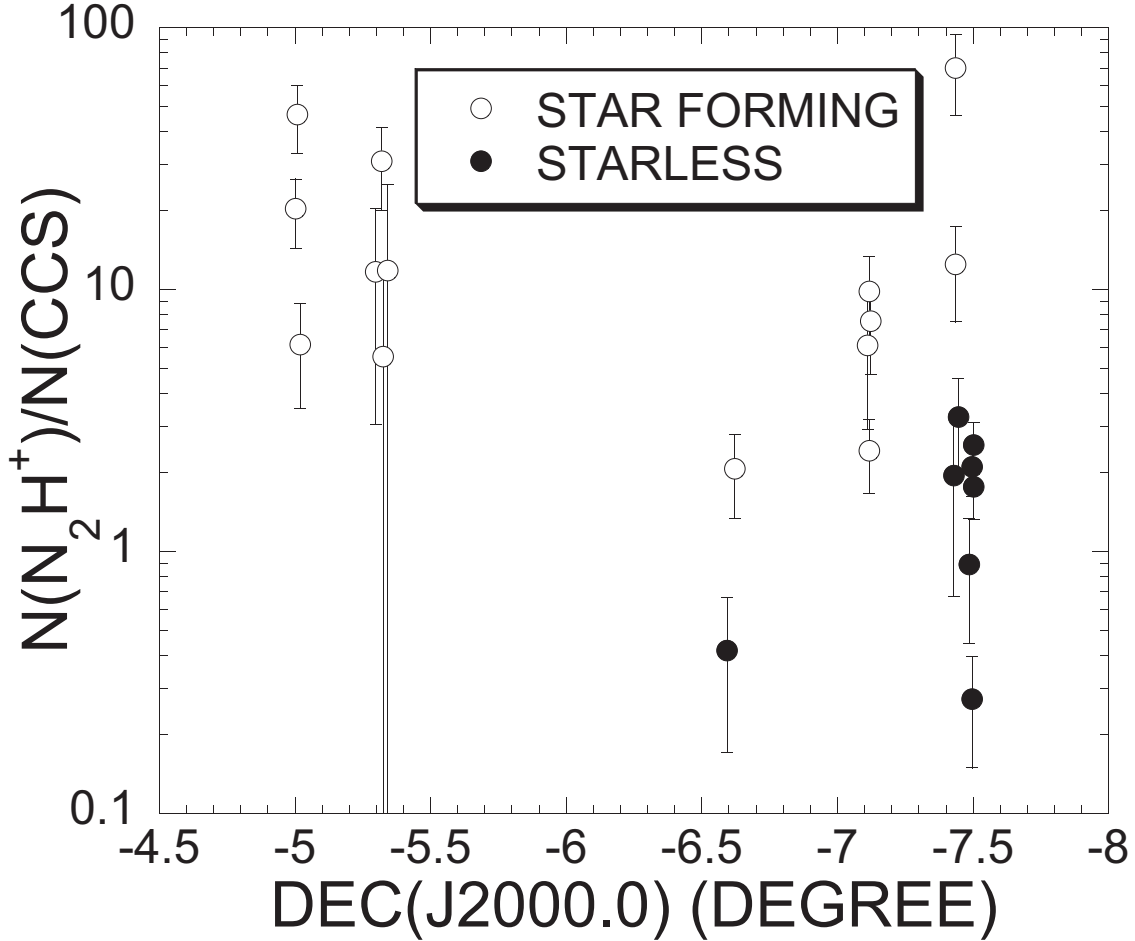


Fig. 22. The ratio of the column density of N_2H^+ to that of CCS is plotted against the declination.

observations. The derived column density of CCS by using the best-fit LVG model is a factor of 4–7 lower than that obtained from the CCS(7-6) line and by assuming LTE conditions. When we take “(Model)”, the absolute intensity at CCS $J_N = 4_3 - 3_2$ tends to be higher than the value observed, although the intensity ratio is close to what was observed. A possibility is that the beam filling factor is lower than unity. Moreover, differences of the beam sizes at these two frequencies do not allow us to make precise estimates of the intensity ratio. Therefore, we will not go to details on the basis of LVG. At least, we conclude that the optical depth of the CCS $J_N = 7_6 - 6_5$ emission is thin or moderate.

3.5. Variation of the N_2H^+/CCS ratio along the Orion A GMC

Tatematsu et al. (2010) found global variation along the Orion A GMC filament in the ratio of the column density of NH_3 to that of CCS. Figure 22 shows the ratio of the column density of N_2H^+ to that of CCS is plotted against declination. Because the observed cores are distributed sparsely, it is hard to derive a tendency. In the northern region (DEC > -6.0 degrees), we only have star-forming peaks.

Tatematsu et al. (2010) did not detect the CCS $J_N = 4_3 - 3_2$ emission at 45.379033GHz toward either Orion KL, which is very warm ($T_k = 70-150$ K: Genzel & Stutzki 1989, Wilson et al. 1999), or the Orion Bar. From Figure 5 of Tatematsu et al. (2010), the detection rate of the CCS $J_N = 4_3 - 3_2$ emission at 45.379033GHz is much lower (15%) for $T_{rot} > 30$ K ($T_k > 40$ K) compared with that in the overall sample (32%). Tatematsu et al. (2008) did not detect the N_2H^+ $J = 1-0$ emission toward the Orion Bar, the archetypal photodissociation region (PDR). The N_2H^+ emission is very weak toward Orion KL. It is known that N_2H^+ $J = 1-0$ traces quiescent molecular gas, which is not affected by star formation activity (e.g., Womack, Ziurys, & Sage 1993). It is possible that both the CCS and N_2H^+ $J = 1-0$ emission is weak in warm, evolved molecular gas.

It is expected that the evolution of clouds in nearby galaxies will become major research topics in near future, because ALMA resolution and sensitivity will allow us to study it in great detail. We believe that our finding on astrochemistry in the Orion A GMC will serve as a basic guide for astrochemical study of GMCs in nearby galaxies by ALMA.

4. Summary

We mapped cores in the Orion A GMC ($T_k \sim 10-30$ K) in CCS $J_N = 7_6 - 6_5$ and N_2H^+ . It is found for cores with temperatures lower than 25 K that the CCS $J_N = 7_6 - 6_5$ emission tends to be strong in starless peaks while the N_2H^+ $J = 1-0$ $F_1 = 2-1$ emission tends to be strong toward protostars. In some cases, we detected local weak CCS $J_N = 7_6 - 6_5$ peaks toward protostars as well as N_2H^+ $J = 1-0$ $F_1 = 2-1$ peaks. This may be caused by secondary late-stage CCS peak in the chemical evolution. The column density ratio of $N(N_2H^+)/N(\text{CCS})$ is low toward starless peaks while it is high toward star-forming peaks. This tendency is consistent with the tendency found in dark clouds ($T_k \sim 10$ K). The criterion found in the Orion A GMC is $N(N_2H^+)/N(\text{CCS}) \sim 2-3$. On the other hand, some protostars do not accompany any N_2H^+ $J = 1-0$ $F_1 = 2-1$ intensity peaks but are associated with dust continuum emitting regions, suggesting that the N_2H^+ abundance might be decreased due to CO evaporation in warmer star-forming sites.

The authors would like to thank an anonymous referee, whose comments greatly improved the paper. J.-E.L. was supported by the Basic Science Research Program through the National Research Foundation of Korea (NRF) funded by the Ministry of Education of the Korean government (grant number NRF-2012R1A1A2044689) and the 2013 Sabbatical Leave Program of Kyung Hee University (KHU-20131724). M.C. was supported by the Core Research Program of National Research Foundation funded by the Ministry of Science, ICT and Future Planning of the Korean government (grant number NRF-2011-0015816).

Table 1. Map Centers and Off Positions

TUKH	Map Center		Off Position		rms (CCS) at 30.52 kHz
	RA(J2000.0)	DEC(J2000.0)	RA(J2000.0)	DEC(J2000.0)	
	h m s	° ' "	h m s	° ' "	
003	5:35:17.7	-5:00:30	5:33:17.2	-5:00:30	0.037
021	5:35:17.2	-5:19:10	5:33:16.7	-5:19:10	0.060
040	5:35:11.7	-5:29:09	5:33:11.1	-5:29:09	0.075
049	5:34:50.1	-5:39:08	5:32:49.5	-5:39:08	0.072
056	5:35:11.1	-5:55:49	5:33:10.5	-5:55:49	0.051
059	5:35:40.4	-6:07:52	5:33:39.7	-6:07:52	0.051
069	5:36:25.8	-6:23:15	5:34:25.1	-6:23:15	0.076
083	5:36:47.0	-6:31:56	5:34:46.2	-6:31:56	0.070
088	5:37:00.4	-6:35:57	5:34:59.6	-6:35:57	0.057
097	5:37:59.0	-7:07:22	5:35:58.1	-7:07:22	0.048
104	5:39:06.2	-7:12:07	5:37:05.2	-7:12:07	0.051
105	5:38:07.0	-7:13:22	5:36:06.0	-7:13:22	0.050
117	5:39:18.4	-7:26:47	5:37:17.4	-7:26:47	0.052
122	5:39:42.5	-7:30:09	5:37:41.5	-7:30:09	0.052

References

- Aikawa Y., Ohashi, N., Inutsuka, S., Herbst, E., & Takakuwa, S. 2001, *ApJ*, 552, 639
- Anglada, G., Rodríguez, L.F., Cantó, J., Estalella, R. & Torrelles, J.M. 1992, *ApJ*, 395, 494
- Benson, P.J., Caselli, P., & Myers, P.C. 1998, *ApJ*, 506, 743
- Beuther, H., Semenov, D., Henning, T., & Linz, H. 2008, *ApJ*, 675, L33
- Caselli, P., Myers, P.C., & Thaddeus, P. 1995, *ApJ*, 455, L77
- Caselli, P., Walmsley, C.M., Tafalla, M., Dore, L., & Myers, P.C. 1999, *ApJ*, 523, L165
- Chini, R., et al. 1997, *ApJ*, 474, L135
- Collings, M. P., Anderson, M. A., Chen, R., et al. 2004, *MNRAS*, 354, 1133
- Evans, N.J., II, Levreault, R.M., & Harvey, P.M. 1986, *ApJ*, 301, 894
- Greene, T.P., Wilking, B.A., André, P., Young, E.T., & Lada, C.J. 1994, *ApJ*, 434, 614
- Genzel, R., & Stutzki, R. 1989, *ARA&A*, 27, 41
- Hirahara, Y., Suzuki, H., Yamamoto, S., Kawaguchi, K., Kaifu, N., Ohishi, M., Takano, S., Ishikawa, S.-I., & Masuda, A. 1992, *ApJ*, 394, 539
- Hirota, T., Ito, T., & Yamamoto, S. 2002, *ApJ*, 565, 359
- Hirota, T., & Yamamoto, S. 2006, *ApJ*, 646, 258
- Hirota, T., Ohishi, M., & Yamamoto, S. 2009, *ApJ*, 699, 585
- Johnstone, D., & Bally, J. 1999, *ApJ*, 510, L49
- Johnstone, D., Boonman, A.M.S., & van Dishoeck, E.F. 2003, *A&A*, 412, 157
- Kim, M.K., et al. 2008, *PASJ*, 60, 991

- Lai, S.-P., & Crutcher, R.M. 2000, *ApJS*, 128, 271
- Levreault, R.M. 1988, *ApJS*, 67, 283
- Lee, H.-H., Herbst, E., Pineau des Foreêts, Roueff, E., & Le Bourlot, J. 1996, *A&A*, 311, 690
- Lee, J.-E., Evans, N.J., II, Shirley, Y.L., & Tatematsu, K. 2003, *ApJ*, 583, 789
- Lee, J.-E., Bergin, E.A., & Evans, N.J., II 2004, *ApJ*, 617, 360
- Li, D., Goldsmith, P.F., & Menten, K. 2003, *ApJ*, 587, 262
- Li, D., Kauffmann, J., Zhang, Q., & Chen, W. 2013, *ApJ*, 768, L5
- Li, Z.-Y., Shematovich, V.I., Wiebe, D.S., & Shustov, B.M. 2002, *ApJ*, 569, 792
- Lis, D.C., Serabyn, E., Dowell, C.D., Benford, D.J., Phillips, T.G., Hunter, T.R., & Wang, N. 1998, *ApJ*, 509, 299
- Maezawa, H., et al. 1999, *ApJ*, 524, L129
- Marka, C., Schreyer, K., Launhardt, R., Semenov, D.A., & Henning, Th. 2012, *A&A*, 537, A4
- Megeath, S.T., et al. 2012, *AJ*, 144, 192
- Myers, P.C. 1983, *ApJ*, 270, 105
- Sakai, T., Oka, T., & Yamamoto, S. 2006, *ApJ*, 649, 268
- Sakai, T., Oka, T., & Yamamoto, S. 2007, *ApJ*, 662, 1043
- Sakai, T., Sakai, N., Kamegai, K., Hirota, T., Yamaguchi, N., Shiba, S., & Yamamoto, S. 2008, *ApJ*, 678, 1049
- Sanhueza, P., Jackson, J.M., Foster, J.B., Garay, G., Silva, A., & Finn, S.C. 2012, *ApJ*, 756, 60
- Suzuki, H., Yamamoto, S., Ohishi, M., Kaifu, N., Ishikawa, S.-I., Hirahara, Y., & Takano, S. 1992, *ApJ*, 392, 551
- Takahashi, S., Ho, P.T.P, Tang, T.-W., Kawabe, R., & Saito, M. 2009, *ApJ*, 704, 1459
- Takahashi, S., Ho, P.T.P, Teixeira, P.S., Zapata, L.A., & Su, Y.-N. 2013, *ApJ*, 763, 57
- Tatematsu, K., et al. 1993a, *ApJ*, 404, 643
- Tatematsu, K., Umemoto, T., Murata, Y., Chen, H., Hirano, N., & Takaba, H. 1993b, *ApJ*, 419, 746
- Tatematsu, K., Kandori, R., Umemoto, T., & Sekimoto, Y. 2008, *PASJ*, 60, 407
- Tatematsu, K., Hirota, T., Kandori, R., & Umemoto, T. 2010, *PASJ*, 62, 1473
- Tiné, S., Roueff, E., Falgarone, E., Gerin, M., & Pineau des Forêts, G. 2000, *A&A*, 356, 1039
- Tsuboi, Y., Koyama, K., Hamaguchi, K., et al. 2001, *ApJ*, 554, 734
- Tsujimoto, M., et al. 2004, *PASJ*, 56, 341
- Turner, B.E. 1988, in *Galactic and Extragalactic Radio Astronomy*, ed. G.L. Vershuur & K.I. Kellermann (2d ed.; New York: Springer-Verlag), 154
- Ungerechts, H., Bergin, E.A., Goldsmith, P.F., Irvine, W.M., Schloerb, F.P., & Snell, R.L. 1997, *ApJ*, 482, 245
- Van der Tak, F.F.S., Black, J.H., Schöier, F.L., Jansen, D.J., & van Dishoeck, E.F., 2007, *A&A*, 468, 627
- Wilson, T.L., Mauersberger, R., Gensheimer, P.D., Muders, D., & Bieging, J.H. 1999, *ApJ*, 525, 343
- Wiseman, J.J., & Ho, P.T.P. 1998, *ApJ*, 502, 676
- Wolkovitch, D., Langer, W.D., Goldsmith, P.F., & Heyer, M., 1997, *ApJ*, 477, 241
- Womack, M., Ziurys, L.M., & Sage, L.J. 1993, *ApJ*, 406, L29

Table 2. Properties of the Young Stellar Objects

Megeath	RA(J2000.0)	DEC(J2000.0)	T_{bol}	Class	α_{IRAC}	L_{bol}	Other Name	Reference for Other Name
	h m s	° ' "	K			L_{\odot}		
545	5:39:19.61	-7:26:18.8	505.3	P	0.34	1.32	Haro 4-255 VLA1	Anglada et al. (1992)
551	5:39:19.98	-7:26:11.2	179.2	P	1.18	1.23	Haro 4-255 FIR	Evans, Levreault, & Harvey
638	5:37:58.76	-7: 7:25.3	176.6	P	2.49	0.08		
640	5:37:57.01	-7: 6:56.5	182.0	P	1.45	0.11		
826	5:37:00.45	-6:37:10.5	643.8	FP	-1	0.02		
1968	5:35:14.93	-5:21: 0.6	1344.3	P		0.08		
1969	5:35:11.84	-5:21: 0.3	716.3	P	-0.15	0.94		
1971	5:35:17.84	-5:20:53.9	1778.1	P		1.11		
2017	5:35:13.60	-5:19:54.9	1245.6	P	0.06	4.44		
2037	5:35:15.39	-5:19:34.4	771.4	P		0.02		
2044	5:35:20.71	-5:19:26.3	780.2	P	0.95	0.81		
2050	5:35:11.61	-5:19:12.4	1407.9	P		0.09		
2060	5:35:22.10	-5:18:57.7	921.5	P		0.06		
2069	5:35:16.69	-5:18:45.2	788.5	P	0.29	0.25		
2073	5:35:12.02	-5:18:40.8	961.3	P		0.03		
2091	5:35:17.09	-5:18:13.9	893.8	P		0.04		
2106	5:35:19.66	-5:17:46.2	779.1	P		0.03		
2427	5:35:23.65	-5: 1:40.3	246.2	P	2.8	0.90	SMM9	Takahashi et al. (2013)
2433	5:35:23.47	-5: 1:28.7	176.9	P	2.35	0.57	MMS6-NE SMM7	Takahashi et al. (2009) Takahashi et al. (2013)
2437	5:35:22.43	-5: 1:14.1	161.6	P	1.76	0.36	MMS5 SMM6	Chini et al. (1997) Takahashi et al. (2013)
2440	5:35:19.96	-5: 1: 2.6	483.7	P	0.4	0.42		
2442	5:35:18.91	-5: 0:50.9	220.8	P		0.18	TKH10 MMS3 SMM4	Tsuboi, Koyama, Hamaguchi Chini et al. (1997) Takahashi et al. (2013)
2446	5:35:18.32	-5: 0:33.0	455.7	P	0.77	6.55	TKH8 MMS2 SMM3	Tsuboi, Koyama, Hamaguchi Chini et al. (1997) Takahashi et al. (2013)
2451	5:35:15.03	-5: 0: 8.2	272.8	P	-0.16	0.10		
2453	5:35:16.15	-5: 0: 2.3	324.6	P	0.39	1.86	CSO3 SMM1	Lis et al. (1998) Takahashi et al. (2013)

Table 3. Intensity Peak, Coordinate, Kinetic Temperature from NH₃, and CCS Line Parameter

TUKH	RA(J2000.0)	DEC(J2000.0)	T_k	T_A^*	LSR Velocity	Δv	rms at 122.08 kHz
	h m s	° ' "	K	K	km s ⁻¹	km s ⁻¹	K
003A	5:35:17.7	-5:00:10	16	0.09 ± 0.02	10.53 ± 0.13	1.69 ± 0.32	0.02
003B	5:35:19.0	-5:00:30	16	0.09 ± 0.02	10.98 ± 0.11	1.18 ± 0.28	0.02
003C	5:35:17.7	-5:01:10	16	0.14 ± 0.02	10.54 ± 0.05	0.75 ± 0.13	0.02
021A	5:35:19.9	-5:17:50	30	0.10 ± 0.02	9.23 ± 0.23	2.65 ± 0.55	0.03
021B	5:35:21.2	-5:18:50	30	0.15 ± 0.03	8.53 ± 0.06	0.54 ± 0.15	0.03
021	5:35:17.2	-5:19:10	30	0.30 ± 0.02	9.30 ± 0.05	1.39 ± 0.12	0.02
021C	5:35:14.5	-5:19:30	30	0.21 ± 0.03	9.03 ± 0.11	1.78 ± 0.25	0.04
021D	5:35:13.2	-5:19:50	30	0.16 ± 0.02	9.15 ± 0.15	2.17 ± 0.35	0.04
021E	5:35:15.9	-5:20:30	30	0.17 ± 0.01	9.77 ± 0.15	2.71 ± 0.36	0.04
088A	5:37:00.4	-6:35:37	24	0.10 ± 0.02	6.50 ± 0.13	1.42 ± 0.30	0.03
088B	5:37:00.4	-6:37:17	24	0.27 ± 0.03	5.97 ± 0.05	0.78 ± 0.11	0.03
088C	5:36:59.1	-6:37:57	24	0.13 ± 0.03	5.79 ± 0.12	1.06 ± 0.30	0.04
097A	5:37:57.7	-7:06:42	10	0.16 ± 0.02	5.80 ± 0.07	1.39 ± 0.17	0.04
097B	5:37:56.3	-7:07:02	10	0.19 ± 0.03	6.11 ± 0.07	0.87 ± 0.16	0.04
097C	5:37:57.7	-7:07:02	10	0.19 ± 0.02	6.14 ± 0.04	0.75 ± 0.10	0.02
097D	5:38:01.7	-7:07:02	10	0.12 ± 0.02	5.41 ± 0.08	0.96 ± 0.18	0.04
097	5:37:59.0	-7:07:22	10	0.16 ± 0.02	5.95 ± 0.06	0.87 ± 0.14	0.02
097E	5:38:00.3	-7:08:02	10	0.15 ± 0.04	6.14 ± 0.05	0.38 ± 0.12	0.03
117A	5:39:22.4	-7:25:47	<10	0.20 ± 0.02	4.22 ± 0.04	0.72 ± 0.09	0.03
117B	5:39:18.4	-7:26:07	<10	0.15 ± 0.03	4.07 ± 0.05	0.51 ± 0.12	0.03
117C	5:39:19.7	-7:26:07	<10	0.09 ± 0.04	4.43 ± 0.09	0.57 ± 0.21	0.02
117D	5:39:17.1	-7:26:27	<10	0.10 ± 0.02	3.88 ± 0.08	0.81 ± 0.18	0.02
117E	5:39:22.4	-7:26:27	<10	0.20 ± 0.03	4.19 ± 0.07	0.87 ± 0.19	0.04
117F	5:39:21.1	-7:26:47	<10	0.19 ± 0.03	4.34 ± 0.04	0.69 ± 0.10	0.03
117G	5:39:19.7	-7:27:07	<10	0.08 ± 0.01	4.48 ± 0.11	1.36 ± 0.29	0.02
122A	5:39:41.2	-7:29:09	<16	0.19 ± 0.03	3.82 ± 0.05	0.57 ± 0.12	0.03
122B	5:39:41.2	-7:29:49	<16	0.22 ± 0.03	3.75 ± 0.02	0.36 ± 0.05	0.01
122C	5:39:42.5	-7:29:49	<16	0.24 ± 0.04	3.78 ± 0.03	0.39 ± 0.08	0.02
122	5:39:42.5	-7:30:09	<16	0.36 ± 0.03	3.74 ± 0.01	0.27 ± 0.03	0.02
122D	5:39:43.8	-7:30:09	<16	0.19 ± 0.03	3.75 ± 0.03	0.39 ± 0.07	0.02
122E	5:39:46.5	-7:30:49	<16	0.26 ± 0.07	3.82 ± 0.03	0.21 ± 0.06	0.03

Table 4. N₂H⁺ Velocity-Integrated Intensity W and Hyperfine Line Fitting

TUKH	W	τ_{TOT}	LSR Velocity	Δv	T_{ex}
	K km s ⁻¹		km s ⁻¹	km s ⁻¹	K
003A	5.6	5.9 ± 1.1	11.18 ± 0.01	0.77 ± 0.04	9.4 ± 0.6
003B	5.8	5.7 ± 1.1	11.05 ± 0.01	0.81 ± 0.04	11.2 ± 0.7
003C	1.8	3.7 ± 1.1	10.46 ± 0.01	0.51 ± 0.02	7.1 ± 0.7
021A	5.8	1.4 ± 0.6	9.29 ± 0.02	1.46 ± 0.07	14.1 ± 3.8
021B	0.8		9.36 ± 0.05		
021	12.5	3.3 ± 0.7	9.73 ± 0.02	1.30 ± 0.06	20.8 ± 1.8
021C	4.0	0.7 ± 0.5	9.44 ± 0.03	2.00 ± 0.09	13.6 ± 6.9
021D	1.8		9.41 ± 0.03	1.54 ± 0.11	
021E	8.2	1.0 ± 0.6	9.94 ± 0.02	1.29 ± 0.06	27.3 ± 12.7
088A	0.5	5.4 ± 2.4	6.53 ± 0.03	0.81 ± 0.09	3.4 ± 0.1
088B	1.4	5.4 ± 1.3	5.80 ± 0.02	0.88 ± 0.06	4.8 ± 0.2
088C	0.1				
097A	2.5	2.9 ± 1.0	5.69 ± 0.02	0.82 ± 0.04	8.5 ± 1.1
097B	1.5	6.9 ± 1.4	6.04 ± 0.01	0.41 ± 0.02	5.4 ± 0.3
097C	2.8	4.2 ± 1.0	5.86 ± 0.02	0.84 ± 0.04	7.5 ± 0.5
097D	0.7				
097	2.1	3.9 ± 1.0	5.77 ± 0.01	0.77 ± 0.04	7.1 ± 0.6
097E	0.7	2.5 ± 1.8	6.12 ± 0.02	0.56 ± 0.04	4.6 ± 1.0
117A	1.4	3.5 ± 1.5	4.50 ± 0.02	0.65 ± 0.04	5.2 ± 0.8
117B	2.9	3.9 ± 1.0	4.76 ± 0.02	0.81 ± 0.04	6.7 ± 0.6
117C	5.1	4.5 ± 1.0	4.65 ± 0.01	0.81 ± 0.04	11.0 ± 0.8
117D	0.6		4.55 ± 0.04	1.00 ± 0.12	4.6 ± 3.0
117E	1.6				
117F	1.4	4.1 ± 1.2	4.42 ± 0.01	0.66 ± 0.03	5.6 ± 0.4
117G	0.4	3.1 ± 2.6	4.38 ± 0.02	0.53 ± 0.05	3.8 ± 0.6
122A	0.6	6.2 ± 2.3	3.95 ± 0.01	0.41 ± 0.03	4.0 ± 0.2
122B	0.4	7.8 ± 2.7	3.85 ± 0.01	0.42 ± 0.03	3.4 ± 0.1
122C	0.9	28.2 ± 5.1	3.82 ± 0.01	0.28 ± 0.01	3.8 ± 0.0
122	0.8	21.8 ± 4.2	3.80 ± 0.01	0.28 ± 0.01	4.1 ± 0.1
122D	0.8	20.3 ± 3.4	3.78 ± 0.01	0.27 ± 0.01	4.0 ± 0.1
122E	0.5				

Table 5. Column Density and Ratios

TUKH	$N(\text{CCS})$	$N(\text{N}_2\text{H}^+)$	$W(\text{N}_2\text{H}^+)/W(\text{CCS})$	$N(\text{N}_2\text{H}^+)/N(\text{CCS})$	Megeath
	cm^{-2}	cm^{-2}			
003A	2.7E+12	5.6E+13 ± 1.0E+13	33.0	20.3 ± 6.0	2453, 2446
003B	1.5E+12	7.1E+13 ± 1.3E+13	54.1	46.5 ± 13.5	2440, 2442, 2446
003C	2.6E+12	1.6E+13 ± 4.7E+12	15.8	6.2 ± 2.7	2442
021A	3.7E+12	4.3E+13 ± 1.8E+13	20.4	11.7 ± 8.6	2106
021B			9.5		2060
021	5.7E+12	1.8E+14 ± 3.8E+13	28.8	30.8 ± 10.8	2069
021C	5.2E+12	2.9E+13 ± 2.1E+13	10.2	5.5 ± 7.1	2037
021D			4.9		2017
021E	6.9E+12	8.1E+13 ± 4.9E+13	16.7	11.8 ± 13.2	1968
088A	5.3E+13	2.2E+13 ± 1.0E+13	3.5	0.4 ± 0.2	
088B	1.4E+13	2.9E+13 ± 7.2E+12	6.5	2.1 ± 0.7	826
088C	2.0E+12		0.6		
097A	4.2E+12	2.6E+13 ± 8.7E+12	10.8	6.1 ± 3.2	640
097B	7.7E+12	1.9E+13 ± 3.9E+12	8.6	2.4 ± 0.8	640
097C	3.3E+12	3.3E+13 ± 7.7E+12	17.7	9.8 ± 3.5	640
097D	5.7E+12		5.9		
097	3.5E+12	2.6E+13 ± 6.6E+12	14.5	7.6 ± 2.8	638
097E	4.3E+12	8.1E+12 ± 5.8E+12	11.5	1.9 ± 1.9	
117A	7.4E+12	1.4E+13 ± 6.4E+12	8.9	1.9 ± 1.3	
117B	2.0E+12	2.6E+13 ± 6.5E+12	36.0	12.5 ± 4.9	545, 551
117C	8.0E+11	5.6E+13 ± 1.2E+13	91.1	70.0 ± 23.6	545, 551
117D	6.0E+12		6.5		
117E	9.0E+12		8.6		
117F	5.6E+12	1.8E+13 ± 5.3E+12	9.4	3.3 ± 1.3	
117G	1.8E+13	8.8E+12 ± 7.4E+12	3.0	0.5 ± 0.5	
122A	1.5E+13	1.4E+13 ± 5.1E+12	5.7	0.9 ± 0.4	
122B	6.2E+13	1.7E+13 ± 5.8E+12	4.5	0.3 ± 0.1	
122C	2.0E+13	4.2E+13 ± 7.6E+12	8.9	2.1 ± 0.5	
122	1.9E+13	3.4E+13 ± 6.5E+12	7.6	1.8 ± 0.4	
122D	1.2E+13	3.0E+13 ± 5.0E+12	9.9	2.5 ± 0.6	
122E	1.2E+12				

Table 6. Best-fit LVG Models for CCS toward TUKH122

Observation or Model	n	T_k	N (CCS)	$T_R(4_3 - 3_2)$	$T_R(7_6 - 6_5)/T_R(4_3 - 3_2)$	$\tau(4_3 - 3_2)$	$\tau(7_6 - 6_5)$
	cm^{-3}	K	cm^{-2}	K			
Observation	0.64	1.38
Model	1E6	10	5E12	0.78	1.18	0.12	0.15
Model	3E6	10	5E12	0.77	1.21	0.11	0.15
Model	1E5	15	5E12	0.83	1.24	0.06	0.16
Model	1E5	20	3E12	0.45	1.55	0.02	0.08
(Model)	1E5	10	2E13	3.0	0.83	0.53	0.77
(Model)	1E5	20	2E13	3.8	1.41	0.14	0.49